The Astrophysical Journal Supplement Series, 252:13 (31pp), 2021 February https://doi.org/10.3847/1538-4365/abd32e

First Fermi-LAT Solar Flare Catalog

M. Ajello[1], L. Baldini[2], D. Bastieri[3,4], R. Bellazzini[5], A. Berretta[6], E. Bissaldi[7,8], R. D. Blandford[9], R. Bonino[10,11], P. Bruel[12], S. Buson[13], R. A. Cameron[9], R. Caputo[14], E. Cavazzuti[15], C. C. Cheung[16], G. Chiaro[17], D. Costantin[18], S. Cutini[19], F. D'Ammando[20], F. de Palma[10], R. Desiante[10], N. Di Lalla[9], L. Di Venere[7,8], F. Fana Dirirsa[21], S. J. Fegan[12], Y. Fukazawa[22], S. Funk[23], P. Fusco[7,8], F. Gargano[8], D. Gasparrini[24,25], F. Giordano[7,8], M. Giroletti[20], D. Green[26], S. Guiriec[14,27], E. Hays[14], J. W. Hewitt[28], D. Horan[12], G. Jóhannesson[29,30], M. Kovac’evic[19], M. Kuss[5], S. Larsson[31,32,33], L. Latronico[10], J. Li[34], F. Longo[35,36], M. N. Lovellette[16], P. Lubrano[19], S. Maldera[10], A. Manfreda[2], G. Martí-Devesa[37], M. N. Mazziotta[8], I. Mereu[6,19], P. F. Michelson[9], T. Mizuno[38], M. E. Monzani[9], A. Morselli[24], I. V. Moskalenko[9], M. Negro[39,40], N. Omodei[9], M. Orienti[20], E. Orlando[9,41], D. Paneque[26], Z. Pei[4], M. Persic[35,42], M. Pesce-Rollins[5], V. Petrosian[9], F. Piron[43], T. A. Porter[9], G. Principe[20], J. L. Racusin[14], S. Rainò[7,8], R. Rando[3,44,45], B. Rani[14,46], M. Razzano[5,52], S. Razzaque[21], A. Reimer[9,37], O. Reimer[37], D. Serini[7], C. Sgrò[5], E. J. Siskind[47], G. Spandre[5], P. Spinelli[7,8], D. Tak[14,48], E. Troja[14,49], J. Valverde[12], K. Wood[50], and G. Zaharijas[41,51]

[1] Department of Physics and Astronomy, Clemson University, Kinard Lab of Physics, Clemson, SC 29634-0978, USA
[2] Università di Pisa and Istituto Nazionale di Fisica Nucleare, Sezione di Pisa I-56127 Pisa, Italy
[3] Istituto Nazionale di Fisica Nucleare, Sezione di Padova, I-35131 Padova, Italy
[4] Dipartimento di Fisica e Astronomia “G. Galilei,” Università di Padova, I-35131 Padova, Italy
[5] Istituto Nazionale di Fisica Nucleare, Sezione di Pisa, I-56127 Pisa, Italy; melissa.pesce.rollins@pi.infn.it
[6] Dipartimento di Fisica, Università degli Studi di Perugia, I-06123 Perugia, Italy
[7] Dipartimento di Fisica “M. Merlin” dell’Università e del Politecnico di Bari, via Amendola 173, I-70126 Bari, Italy
[8] Istituto Nazionale di Fisica Nucleare, Sezione di Bari, I-70126 Bari, Italy
[9] W. W. Hansen Experimental Physics Laboratory, Kavli Institute for Particle Astrophysics and Cosmology, Department of Physics and SLAC National Accelerator Laboratory, Stanford University, Stanford, CA 94305, USA; nicola.omodei@stanford.edu, vahep@stanford.edu
[10] Istituto Nazionale di Fisica Nucleare, Sezione di Torino, I-10125 Torino, Italy
[11] Dipartimento di Fisica, Università degli Studi di Torino, I-10125 Torino, Italy
[12] Laboratoire Leprince-Ringuet, École polytechnique, CNRS/IN2P3, F-91128 Palaiseau, France
[13] Institut für Theoretische Physik und Astrophysik, Universität Würzburg, Campus Hubland Nord, Emil-Fischer-Str. 31, D-97074 Würzburg, Germany
[14] NASA Goddard Space Flight Center, Greenbelt, MD 20771, USA
[15] Italian Space Agency, Via del Politecnico snc, I-00133 Roma, Italy
[16] Space Science Division, Naval Research Laboratory, Washington, DC 20375-5352, USA
[17] INAF-Istituto di Astrofisica Spaziale e Fisica Cosmica Milano, via E. Bassini 15, I-20133 Milano, Italy
[18] University of Padua, Department of Statistical Science, Via 8 Febbraio, 2, 35122 Padova, Italy
[19] Istituto Nazionale di Fisica Nucleare, Sezione di Perugia, I-06123 Perugia, Italy
[20] INAF Istituto di Radioastronomia, I-40129 Bologna, Italy
[21] Department of Physics, University of Johannesburg, PO Box 524, Auckland Park 2006, South Africa
[22] Department of Physical Sciences, Hiroshima University, Higashi-Hiroshima, Hiroshima 739-8526, Japan
[23] Friedrich-Alexander Universität Erlangen-Nürnberg, Erlangen Centre for Astroparticle Physics, Erwin-Rommel-Str. 1, D-91058 Erlangen, Germany
[24] Istituto Nazionale di Fisica Nucleare, Sezione di Roma “Tor Vergata,” I-00133 Roma, Italy
[25] Space Science Data Center - Agenzia Spaziale Italiana, Via del Politecnico, snc, I-00133, Roma, Italy
[26] Max-Planck-Institut für Physik, D-80805 München, Germany
[27] The George Washington University, Department of Physics, 725 21st St NW, Washington, DC 20052, USA
[28] University of North Florida, Department of Physics, 1 UNF Drive, Jacksonville, FL 32224, USA
[29] Science Institute, University of Iceland, IS-107 Reykjavik, Iceland
[30] Nordita, Royal Institute of Technology and Stockholm University, Roslagstullsbacken 23, SE-106 91 Stockholm, Sweden
[31] Department of Physics, KTH Royal Institute of Technology, AlbaNova, SE-106 91 Stockholm, Sweden
[32] The Oskar Klein Centre for Cosmoparticle Physics, AlbaNova, SE-106 91 Stockholm, Sweden
[33] School of Education, Health and Social Studies, Natural Science, Dalarna University, SE-791 88 Falun, Sweden
[34] Deutsches Elektronen Synchrotron DESY, D-15738 Zeuthen, Germany
[35] Istituto Nazionale di Fisica Nucleare, Sezione di Trieste, I-34127 Trieste, Italy; francesco.longo@trieste.infn.it
[36] Dipartimento di Fisica, Università di Trieste, I-34127 Trieste, Italy
[37] Institut für Astro- und Teilchenphysik, Leopold-Franzens-Universität Innsbruck, A-6020 Innsbruck, Austria
[38] Hiroshima Astrophysical Science Center, Hiroshima University, Higashi-Hiroshima, Hiroshima 739-8526, Japan
[39] Center for Research and Exploration in Space Science and Technology (CRESST) and NASA Goddard Space Flight Center, Greenbelt, MD 20771, USA
[40] Department of Physics and Center for Space Sciences and Technology, University of Maryland Baltimore County, Baltimore, MD 21250, USA
[41] Istituto Nazionale di Fisica Nucleare, Sezione di Trieste, and Università di Trieste, I-34127 Trieste, Italy
[42] Osservatorio Astronomico di Trieste, Istituto Nazionale di Astrofisica, I-34143 Trieste, Italy
[43] Laboratoire Univers et Particules de Montpellier, Université Montpellier, CNRS/IN2P3, F-34095 Montpellier, France
[44] Department of Physics and Astronomy, University of Padova, Vicolo Osservatorio 3, I-35122 Padova, Italy
[45] Center for Space Studies and Activities “G. Colombo,” University of Padova, Via Venezia 15, I-35131 Padova, Italy
[46] Korea Astronomy and Space Science Institute, 776 Daedeokdae-ro, Yuseong-gu, Daejeon 30455, Korea
[47] NYCB Real-Time Computing Inc., Lattingtown, NY 11560-1025, USA
[48] Department of Physics, University of Maryland, College Park, MD 20742, USA
[49] Department of Astronomy, University of Maryland, College Park, MD 20742, USA
[50] Praxis Inc., Alexandria, VA 22303, USA
[51] Center for Astrophysics and Cosmology, University of Nova Gorica, Nova Gorica, Slovenia
Received 2020 July 23; revised 2020 November 30; accepted 2020 December 6; published 2021 January 20

[52] Funded by contract FIRB-2012-RBFR12PM1F from the Italian Ministry of Education, University and Research (MIUR).
[53] Resident at Naval Research Laboratory, Washington, DC 20375, USA.

Abstract

We present the first Fermi-Large Area Telescope (LAT) solar flare catalog covering the 24th solar cycle. This catalog contains 45 Fermi-LAT solar flares (FLSFs) with emission in the γ-ray energy band (30 MeV–10 GeV) detected with a significance of ≳5σ over the years 2010–2018. A subsample containing 37 of these flares exhibits delayed emission beyond the prompt-impulsive hard X-ray phase, with 21 flares showing delayed emission lasting more than two hours. No prompt-impulsive emission is detected in four of these flares. We also present in this catalog observations of GeV emission from three flares originating from active regions located behind the limb of the visible solar disk. We report the lightcurves, spectra, best proton index, and localization (when possible) for all FLSFs. The γ-ray spectra are consistent with the decay of pions produced by >300 MeV protons. This work contains the largest sample of high-energy γ-ray flares ever reported and provides a unique opportunity to perform population studies on the different phases of the flare and thus allowing a new window in solar physics to be opened.

Unified Astronomy Thesaurus concepts: Solar flares (1496); Solar gamma-ray emission (1497); Gamma-ray sources (633); Gamma-ray telescopes (634); Catalogs (205)

1. Introduction

It is generally accepted that the magnetic energy released through reconnection during solar flares is capable of accelerating electrons and ions to relativistic energies on timescales as short as a few seconds. Much is known of the electron acceleration during these explosive phenomena thanks to the observations made in hard X-rays (10 keV–1 MeV; HXRs; see, e.g., Vilmer 1987; Dennis 1988; Lin & Team 2003) and microwaves (see, e.g., Trottet et al. 1998). The observed impulsive-phase radiation in solar flares is dominated by electron emission; however, a fair fraction of stronger flares, with longer impulsive phase, show even higher-energy emission at γ-ray energies (E > 3 MeV) by accelerated protons and other ions in the form of nuclear de-excitation lines and by ~3–50 MeV ions, and >100 MeV continuum due to the decay of pions produced by >300 MeV ions (see, e.g., Vilmer et al. 2011). The first reported observation of γ-rays with energies above 10 MeV was made in 1981 with the Solar Maximum Mission (SMM) spectrometer (Chupp et al. 1982) and throughout the 1980s, several other observations were made (see, e.g., Forrest et al. 1985, 1986), providing evidence of pion-decay emission and revealing multiple phases in the flares.

The first detection of GeV γ-rays was made by the Energetic Gamma-Ray Experiment Telescope (EGRET) on board the Compton Gamma-Ray Observatory (CGRO; see, e.g., Kanbach et al. 1993; Vilmer et al. 2003). The majority of the flares observed from 50 MeV to 2 GeV by EGRET had durations lasting tens of minutes but up to several hours in two flares, leading to a new class of flares initially known as long-duration gamma-ray flares (Ryan 2000; Chupp & Ryan 2009). This new class of flares presented a challenge to the classical magnetic reconnection theory for particle acceleration during flares because the γ-ray emission persisted beyond any other flare emissions, therefore suggesting the need for an additional mechanism and site for acceleration of protons and other ions. However, with only two such detections, the search for an additional acceleration mechanism and site was very challenging.

Additional cases suggesting the need for a new source of ion acceleration came with the observations of γ-ray emission, up to only 100 MeV, from three flares whose host active regions (ARs) were located behind the limb (BTL) of the visible solar disk (Vestrand & Forrest 1993; Barat et al. 1994; Vilmer et al. 1999). It is generally believed that lower-energy γ-rays are produced at the dense footpoints of flare loops by ions accelerated at the reconnection regions near the top of these loops. Thus, observations of BTL flares pose interesting questions regarding the acceleration site and mechanism of the ions and about their transport to the high-density photospheric regions on the visible disk. Although there were some scenarios put forth (Cliver et al. 1993), no convincing explanations were given for the acceleration and transport sites and mechanisms of particles responsible for these observations.

Prior to the launch of the Fermi Gamma-ray Space Telescope in 2008, the understanding of these emission mechanisms was severely limited because of the limited amount of high-energy γ-ray flares detected.

The Fermi-Large Area Telescope (LAT; Atwood et al. 2009) observations of the flaring Sun over its first 12 years in orbit have revealed an extremely rich and diverse sample of events, spanning from short prompt-impulsive flares (Ackermann et al. 2012b) to the gradual-delayed long-duration phases (Ackermann et al. 2014), including the longest extended emission ever detected (~20 hr) from the SOL2012 March 7, a Geostationary Operational Environmental Satellite (GOES) X-class flare (Ajello et al. 2014).[54] The LAT, thanks to its large field of view (FoV) of 2.4 sr, monitors the entire sky every two orbits as an excellent general-purpose γ-ray astrophysics observatory, but in doing so, it keeps the Sun in the FoV 40% of the time. Nonetheless, thanks to its technology improvements with respect to previous γ-ray space-based missions, the Fermi-LAT has increased the total number of >30 MeV detected solar flares by almost a factor of 10. More importantly, the LAT with its higher spatial resolution than EGRET can localize the centroids of the γ-ray emissions on the photosphere, which is particularly important for the interpretation of the BTL flares.

In this Fermi-LAT Solar Flare (FLSF) catalog, we present the observations of 45 flares with >30 MeV emission in the period 2010 January–2018 January (covering most of the 24th solar cycle). From these observations, we now know that >100 MeV γ-ray emission from even moderate GOES-class flares is fairly common (roughly half of the FLSFs in our catalog are associated with M-class flares) and that this high-energy emission is not correlated with the intensity of the X-ray flare, as one might expect. Our spectral analysis indicates that the >100 MeV emission is due to accelerated ions as opposed to HXR and microwave producing electrons. Based on the timing evolution of the γ-ray emission, we find that there are

[54] Solar flares observed by the GOES are classified, on the basis of their peak flux in the soft X-ray range of 0.5–10 keV, as X, M, C, and A class with peak fluxes greater than 10^{-4}, 10^{-5}, 10^{-6}, and 10^{-7} Watt m^{-2}, respectively.

two main populations of γ-ray flares: impulsive prompt (prompt hereafter) and gradual delayed (delayed hereafter). The prompt flares are those whose emission evolution is similar to that of the HXRs, indicating common acceleration sites and mechanism of electrons and ions. The emission of delayed FLSFs, which are always (with the exception of FLSF 2012 October 23 and FLSF 2012 November 27) associated with fast coronal mass ejections (CMEs), rises at the end of the impulsive HXR phase and, like solar energetic particles (SEPs), extends well beyond the end of the HXR emission (for up to tens of hours). This and other observations suggest a different acceleration site and mechanism.

In Section 2, we describe the analysis methods and procedures used in this work, which includes the description of an automated pipeline (Section 2.1), the LAT Low Energy (LLE) analysis (Section 2.2), spectral analysis (Section 2.3), how we perform our localization of the γ-ray emission (Section 2.4), and the search for spatial extension in the γ-ray emission of the brightest flares (Section 2.5). Here we also describe the methods used to calculate the total emission, fluence, and the total number of accelerated >500 MeV protons needed to produce the observed emission (Section 2.6). In Section 3, we describe how solar flares are classified based on the evolution of their γ-ray emission. In Section 4, we present the results of the catalog. In Section 5, we discuss the main findings of this work and the theoretical implications of our results. The tables and figures for each individual flare in this catalog are reported at doi:10.5281/zenodo.4311156.

2. Analysis Methods and Procedures

The LAT is sensitive to γ-rays in the energy range between 30 MeV and >300 GeV (Atwood et al. 2013). The LAT registers energy, direction, and time information for each detected particle. Each such “event” is classified by on-ground processing as a photon or other particle based on the consistency of its interaction with that expected from energetic γ rays.

Event classes correspond to different levels of purity tolerance of the γ-ray sample appropriate for use in different types of analyses. For each event class, there is a corresponding set of Instrument Response Functions (IRFs) describing the performance of the instrument. The standard analysis and software are described at the Fermi Science Support Center (FSSC) website[55] and, in great detail, in Ackermann et al. (2012a).

For the FLSF catalog, we developed two analysis chains, the first one, which we call standard, uses data with energies between 60 MeV and 10 GeV from two sets of event classes, P8R3_SOURCE and the solar flare Transient class P8R3_TRANSIENT015s (S15).[56] The P8R3_SOURCE (Bruel et al. 2018) class is the event class recommended for the standard Fermi-LAT source analysis, while the S15 class was specifically developed to be insensitive to the potential pulse pile-up in the anti-coincidence detector (ACD) scintillators of the LAT resulting from the intense flux of X-rays during the prompt phase of solar flares. Pile-up of X-rays during the readout integration time of the ACD coincident with the entry of a γ ray into the LAT can cause the otherwise good γ ray to be misidentified as a charged particle by the instrument flight software or event-classification ground software and thereby mistakenly vetoed. The Fermi-LAT instrument team closely monitors this effect and tags time intervals with particularly high activity in the sunward ACD tiles as “bad time intervals” (BTI) in the public data archive.[57] The S15 event class is robust against these spurious vetoes because it is defined using selections that exclude variables associated with the ACD and are therefore less susceptible to X-ray pile-up activity which can occur during the impulsive phase of solar flares; thus, all analysis in this catalog during a BTI used the S15 event class.

Additionally, a subset of results on short-duration prompt solar flares was obtained using the second chain based on LLE analysis methods. The LLE technique is an analysis method designed to study bright transient phenomena, such as gamma-ray bursts and solar flares, in the 30 MeV–1 GeV energy range. The LAT collaboration developed this analysis using a different approach from that used in the standard photon analysis. The idea behind LLE is to maximize the effective area below ~1 GeV by relaxing the standard analysis requirement on background rejection; see Ajello et al. (2014) for a full description of the LLE method. The LAT collaboration has already used the LLE technique to analyze solar flares, in particular FLSF 2010 June 12 (the first flare detected by the LAT; see Ackermann et al. 2012b) and the prompt phase of the FLSF 2012 March 7 flares (Ajello et al. 2014). In this FLSF catalog, we used the LLE selection to study the short prompt phase of 14 solar flares.

These two approaches are complementary: the LLE method suffers from large background contamination and is effective only for short transients but, because it is much less restrictive than the P8R3_SOURCE event class, the LLE class has a much larger effective area and has significantly greater sensitivity at high incidence angles.

Indeed, the FLSF 2010 June 12 was detected with the LLE approach when the Sun was more than 75° off-axis (Ackermann et al. 2012b).

2.1. The Fermi-LAT SunMonitor

We have created an automated data analysis pipeline, the Fermi-LAT SunMonitor, to monitor the high-energy γ-ray flux from the Sun throughout the Fermi mission.[58] The time intervals during which we run the analysis are when the Sun is <70° from the LAT boresight.

The effective area of the LAT decreases significantly for sources at incidence angles larger than 60°, so only very bright transients are detectable past this limit. Selecting a maximum off-axis angle of 70° extends the window of continuous Sun exposure for the brightest flares. The duration of these windows varies (ranging from 5 to 80 minutes, with an average duration of 30 minutes, as is shown in Figure 1) as the Sun advances along the ecliptic and as the orbit of Fermi precesses. Contamination from γ rays produced by cosmic-ray interactions with Earth’s atmosphere is reduced by selecting only events arriving within 100° of the zenith.[59]

Each interval is analyzed using an RoI of 10° radius, centered on the position of the Sun at the central time of the

[55] http://fermi.gsfc.nasa.gov/ssc/

[56] Events belonging to the P8R_TRANSIENT015s class are available in the extended photon data through the Fermi Science Support Center.

[57] http://fermi.gsfc.nasa.gov/ssc/data/access/

[58] Results from this pipeline are available online at https://hesperia.gsfc.nasa.gov/fermi_solar/.

[59] We used the gtmktime filter cut=(DATA_QUAL>0||DATA_QUAL==-1) LAT_CONFIG==1 angsep(R.A._ZENITH,decl._ZENITH,R.A., decl.) < (zmax-rad), where R.A. and decl. are those of the position of the Sun at the time of the flare, zmax = 100° and rad is the radius of the region of interest (RoI) used for the analysis.

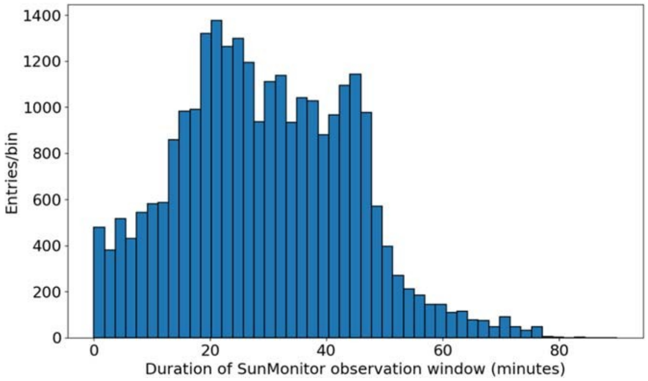

Figure 1. Duration of the Fermi SunMonitor observation windows. The duration varies from 5 to 80 minutes with an average duration of 30 minutes.

interval. On average, the duration of a SunMonitor interval is 30 minutes. During this time, the maximum deviation of the true position of the Sun from the RoI center due to its apparent motion is ~0°. 02. This is smaller than the typical angular resolution of the instrument: the 68% containment angle of the reconstructed incoming γ-ray direction for normal incidence at 1 GeV is 0°. 8 and at 100 MeV is 5°. Furthermore, the statistical uncertainty on the measured centroid of the >100 MeV emission is always larger than 0°. 03, even for the brightest solar flares. It is therefore not necessary to apply a correction to account for the motion of the Sun from the center of the RoI. In each SunMonitor interval, we perform an unbinned maximum likelihood analysis using the tools in the Fermi ScienceTools software package.[60] The unbinned analysis computes the log-likelihood of the data using the reconstructed direction and energy of each individual γ-ray and the assumed sky model folded through the instrument response functions corresponding to the selected event class.

The likelihood analysis consists of maximizing the probability of obtaining the data given an input model as well as deriving error estimates. The RoI is modeled with a solar component and two templates for diffuse γ-ray background emission: a galactic component produced by the interaction of cosmic rays with the gas and interstellar radiation fields of the Milky Way, and an isotropic component that includes both the contribution of the extragalactic diffuse emission and the residual cosmic rays that passed the γ-ray classification.[61] We fix the normalization of the galactic component but leave the normalization of the isotropic background as a free parameter to account for variable fluxes of residual cosmic rays.

When the Sun is not flaring, it is a steady, faint source of γ rays. This emission consists of two components: a disk emission originating from hadronic cosmic-ray cascades in the solar atmosphere and a spatially extended emission from the inverse Compton scattering of cosmic-ray electrons on solar photons in the heliosphere. The disk emission was first mentioned by Dolan & Fazio (1965) and Seckel et al. (1991), and the existence of an additional, spatially extended component was not realized until recently (Moskalenko et al. 2006; Orlando & Strong 2007; Linden et al. 2018; Mazziotta et al. 2020). The quiet Sun was detected for the first time in γ rays in the EGRET data (Orlando & Strong 2008). We also include the quiet Sun emission disk component as a point source in our RoI; however, we did not include the extended inverse Compton (IC) component described in Abdo et al. (2011) because it is too faint to be detected during these time intervals. The >100 MeV flux of the solar disk component used in the FLSF catalog, obtained during the first 18 months of Fermi-LAT observations (Abdo et al. 2011), is 4.6 ($\pm 0.2^{\rm stat} \pm 1.0^{\rm syst}$) $\times 10^{-7}$ ph cm^{-2} s^{-1}.

We rely on the likelihood ratio test and the associated test statistic (TS; Mattox et al. 1996) to estimate the significance of the detection. Here we define TS as twice the increment of the logarithm of the likelihood obtained by fitting the data with the source and background model component simultaneously with respect to a fit with only the background. Note that the significance in σ for the 68% confidence interval can be roughly approximated as $\sqrt{\rm TS}$.

With a pipeline testing for detection in so many time windows (33,511 total over the period of this work), we need to account for the trials factor to understand the statistical significance of a γ-ray source detected in the SunMonitor with a particular value of TS.

Assuming each window is independent, a TS of 20, which would otherwise correspond to a confidence of about 4.5σ, corresponds to 1.38σ post-trials. In order to have a detection significance of 5σ, we must impose a cut on the TS with a minimum of 30. This corresponds to a selection of 133 time windows, some of them consecutive in time for solar flares lasting more than an hour. Following this systematic sweep with SunMonitor, a detailed analysis is performed on those windows with a TS above 30.

From 2010 January to the end of 2018 January, we applied the SunMonitor pipeline analysis to 33,511 intervals of duration longer than 5 minutes. The cases when the duration is less than 5 minutes are likely due to the RoI being close to the maximum zenith angle or cut short by a passage of the satellite into the South Atlantic Anomaly (SAA). These are generally not long enough to yield a reliable point-source likelihood detection and constrain the background. Overall, the Sun was observable for an average duty cycle of 28% for the entire timespan of the FLSF catalog.

Note that outside the time interval considered here, since 2018 April, the LAT has been operating with a modified observing profile due to a failure of one of the solar array drive assemblies that reduce its exposure to the Sun.[62] This change in observing strategy results in an average 45% reduction in solar exposure for the standard event classes (22% reduction for LLE) and consequently in the potential for solar physics science with the LAT.

2.2. LAT Low-energy Spectral Analysis

The LLE technique is designed to study bright transient phenomena, such as solar flares, in the 30 MeV–1 GeV energy range. In this catalog, we used the LLE selection to study the prompt phase of 14 solar FLSFs. To obtain the LLE spectral data, we used the gtburst package, available in the Fermitools distribution from the FSSC. The LLE data are divided by gtburst in 50 logarithmically spaced energy bins from 10 MeV to 10 GeV. For the spectral analysis, we used only the bins in the energy range optimized for the LLE selection.

[60] We used version 2011 May 3 available at http://fermi.gsfc.nasa.gov/ssc/.

[61] The models used for this analysis, gll_iem_v07.fits and iso_P8R3_SOURCE_V2_v1.txt, are available at http://fermi.gsfc.nasa.gov/ssc/data/access/lat/BackgroundModels.html.

[62] See https://fermi.gsfc.nasa.gov/ssc/observations/types/post_anomaly/ for more information.

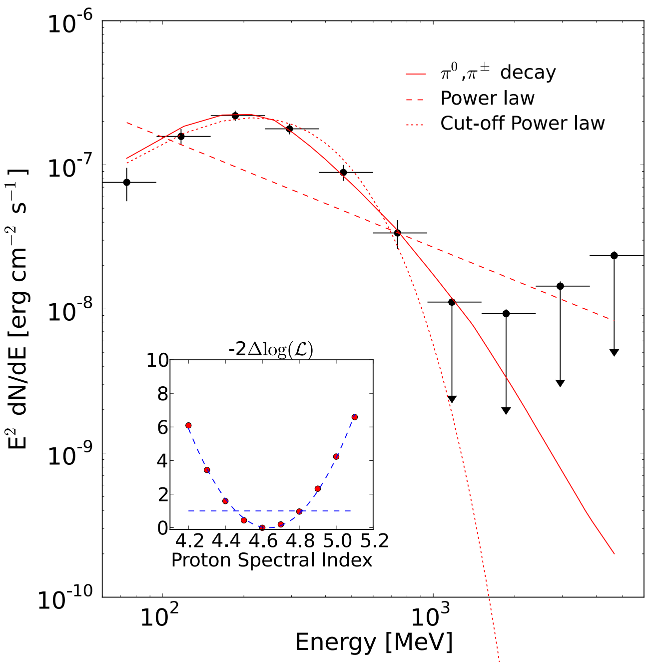

Figure 2. Example γ-ray spectra for SOL2012 March 7. The data were fit with three models (PL, PLEXP, and pion templates) and when the curved model (PLEXP) is preferred to the PL model, we perform a scan over the pion templates to search for the best proton index. In the inset, we show the fit to the log-likelihood values with a parabola, and the 68% confidence level is indicated by the straight line at $-2\Delta\log(\mathcal{L}_{min}) + 1$.

A spectral fit was then performed using the XSPEC (Arnaud 1996) package following an approach similar to the one previously adopted for the analysis of the prompt phase of SOL2012 March 7 (Ajello et al. 2014). The results of the joint analysis with the Fermi Gamma-ray Burst Monitor (GBM) Bismuth-Germanate (BGO) data (300 keV–20 MeV) will be reported in a forthcoming publication.

2.3. Spectral Analysis

We fit three models to the Fermi-LAT γ-ray solar spectral data. The first two, a simple power law (PL) and a power-law with an exponential cutoff (PLEXP), are phenomenological functions that may describe bremsstrahlung emission from relativistic electrons. The parameters of these models are varied to obtain the best fit to the data. When the PLEXP provides a significantly better fit than the PL, we also fit the data with a third model consisting of pion-decay emission templates.[63] This third model uses a series of γ-ray spectral templates derived from a detailed study of γ rays from the decay of pions produced by interactions of accelerated protons and ions with background protons and ions. The accelerated particles are assumed to have a power-law energy spectrum ($dN/dE \propto E^{-\beta}$), where E is the kinetic energy of the protons with index β and an isotropic pitch angle distribution, injected into a thick target with a coronal composition (Reames 1995) taking He/H = 0.1 (updated from Murphy et al. 1987).

When the PLEXP provides a significantly better fit than the PL, we fit the data with the pion templates to determine the proton index that best fits the data. To do this, we calculate the variation of the log-likelihood with the proton spectral index and fit it with a parabola. We run the likelihood analysis for each of the 41 proton spectral indices available from our templates (2.0–6.0 in steps of 0.1). The minimum of this distribution ($\mathcal{L}_{min}$) gives the best-fit spectral index and the corresponding value $\mathcal{L}_0$ as the maximum likelihood. Figure 2 shows an example of a spectral energy distribution of SOL2012 March 7 obtained following this procedure.

Once we have found the proton index corresponding to the best fit and the value of the observed γ-ray emission, we can estimate the total number of >500 MeV accelerated protons (N500 hereafter) needed to produce the observed γ-ray emission over a given time following the prescription of Murphy et al. (1987).

To compute the photon spectral energy distribution, we divide the data into 10 energy bins (in the energy range 60 MeV–10 GeV) and determine the source flux using the unbinned maximum likelihood algorithm gtlike, keeping the normalization of the background constant at the best-fit value and assuming that the spectrum of the point source is an E^2 power law. For nondetections (TS < 9), we compute 95% CL upper limits.

2.4. Localizing the Emission from Fermi-LAT Solar Flares

The standard tool for studying the localization of γ-ray sources with an unbinned likelihood analysis is the gtfindsrc algorithm from ScienceTools.[64] The likelihood analysis is based on sky models with background sources at fixed spatial positions and the best spectral fit for the source of interest. gtfindsrc uses a multidimensional minimization of the unbinned likelihood for a grid of positions around an initial guess until the convergence tolerance for a positional fit is reached. However, the Sun is in the FoV of the LAT for relatively short timescales, which can result in inhomogeneous exposure across the FoV. For this reason, we relied on the gttsmap algorithm to study the localization for the FLSFs of the catalog. The TS maps are created by moving a putative point source through a grid of locations on the sky and maximizing –log(likelihood) at each grid point, with any other well-identified sources within the RoI included in each fit. The solar flare source is then identified at the local maximum of the TS map. The 68% containment radius (or 1σ statistical localization error) on the position corresponds to a drop in the TS value of 2.30 (4.61 and 9.21 correspond to 2σ and 3σ, respectively). See Figure 3 for an example TS map of FLSF 2017 September 10.

When performing the localization of the Fermi-LAT data of the Sun it is necessary to also take into account the fish-eye effect. The fish-eye effect is a selection bias in the LAT trigger and reconstruction algorithms. At low energies and high incidence angles, particles that scatter toward the LAT boresight (having a smaller apparent incidence angle) are reconstructed with higher efficiency than particles that scatter away from the LAT boresight (having a larger apparent incidence angle). The reconstructed position of the source is biased and ends up appearing closer to the boresight axis than its true position.

The fish-eye effect can be quantified on an event-by-event basis using Monte Carlo simulations. The correction depends both on the true incidence angle and the energy of the particle. The correction becomes dramatic at energies below 100 MeV

[63] We are using only pion-production emission, ignoring other (minor) components that contribute to the γ-ray emission.

[64] Available at http://fermi.gsfc.nasa.gov/ssc/data/analysis/software/.

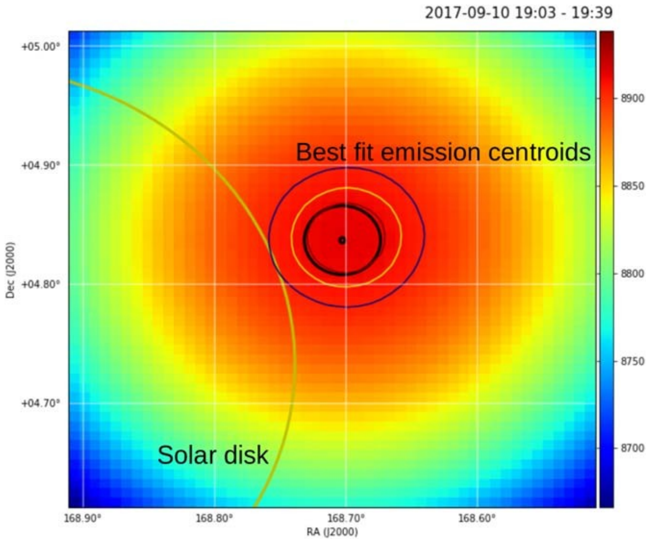

Figure 3. TS map for the observation of FLSF 2017 September 10 in the time interval of 19:03–19:39 UT. The large yellow circle represents the solar disk, the solid black circle represents the 68% statistical error. The thin red, yellow, and blue lines track the 1σ, 2σ, and 3σ contours on the TS map. These are not always perfectly circular, but a circular error containment region (black circle) provides a good approximation.

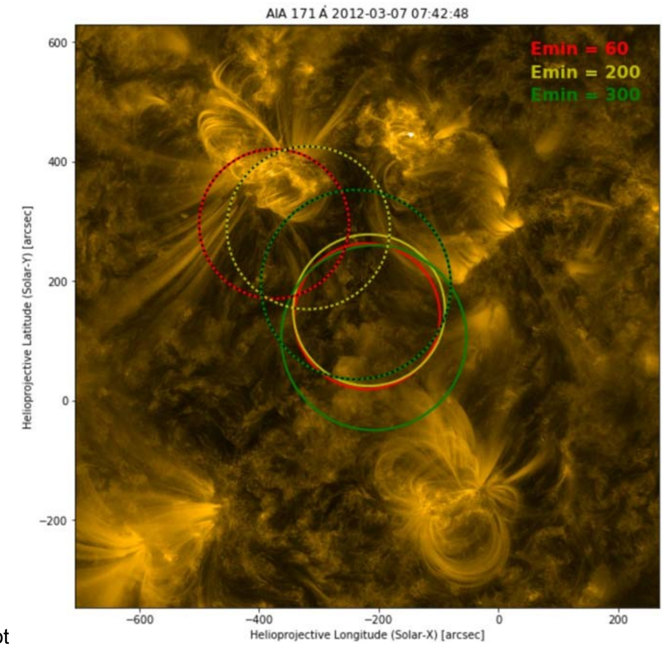

Figure 4. Comparison of the localization of the bright FLSF 2012 March 7 between fish-eye corrected (solid line) and not corrected (dashed line) with 60 (red), 200 (yellow), and 300 (green) MeV energy thresholds. Each circle marks the 68% statistical containment radius. The background is an Atmospheric Imaging Assembly (AIA) 171 Å image taken on 2012 March 7 07:42:48 UT by the Solar Dynamics Observatory (SDO).

and incidence angle greater than 70°, reaching several degrees shift (see Ackermann et al. 2012a for a detailed description of the fish-eye effect).

The correction of the fish-eye effect is crucial particularly for bright flares, when the statistical error on the position becomes smaller than 0°.1 and the uncertainty becomes dominated by systematics. We investigated the effect of the fish-eye correction on two bright solar flares (FLSF 2012 March 7 and FLSF 2017 September 10). We varied the value of the minimum energy threshold to quantify the amplitude of the correction and the systematic error it induces. The amplitude of the fish-eye correction decreases with energy so we expect the distance between the corrected and uncorrected positions to decrease with energy. This is indeed what we observe in Figure 4: the correction is largest above a 60 MeV minimum energy, and above 300 MeV the two positions are consistent.

Solar flares generally have soft γ-ray spectra, cutting off at energies just above 100 MeV, so that the localization error (statistical) does not really improve as the threshold energy is increased, as can be seen in an example in Figure 4, where the statistical error on the localization above 300 MeV (green) is larger than the one above 60 MeV (red). Due to this, we use only photons with measured energies above 100 MeV when performing the localization study. Note that, although the localization uncertainties at 60 and 100 MeV are very similar, the fish-eye correction that we had to apply to the events between 60 and 100 MeV is larger than the one for the events above 100 MeV; therefore, in order to minimize the systematic uncertainty, we use only events with energy >100 MeV to estimate the localization of the emission.

2.4.1. Localization of BTL FLSF 2014 September 1

The emission centroid for the other FLSFs previously published all remained within the 68% error radius with the new analysis tool; the FLSF 2014 September 1 is the only exception that we found during the analysis performed for this work.

As mentioned in Section 2.4, the tool used to perform localization studies for the FLSF catalog to compensate for the potential systematic errors tied to inhomogeneous exposures across the FoV for short detections is gttsmap and no longer the gtfindsrc tool. We also reported (in Section 2.4) the study performed to quantify the impact on the localization results due to the fish-eye effect and showed that it depends on the energy and incidence angle of the source. For this reason, in the FLSF catalog, we have decided to perform localization studies using gttsmap on bright flares with exposure times longer than 20 minutes, with incidence angles smaller than 60° and with energies greater than 100 MeV in order to avoid potentially large systematic effects in the resulting emission centroids.

The first detection window of the BTL FLSF 2014 September 1 unfortunately occurred when the Sun was at an angle of 67° from the LAT boresight and lasted for only 16 minutes and the emission centroid published in Ackermann et al. (2017) was obtained using the gtfindsrc tool. After a careful reanalysis of this flare with the new localization tool and the knowledge obtained from the fish-eye systematic study, we find that the emission centroid for FLSF 2014 September 1 has moved with respect to the previously published value as can be seen in Figure 5.

2.5. Test for Spatial Extension

We test the possibility of measuring spatial extension in the localization results of the bright FLSF 2012 March 7 and FLSF 2017 September 10 by using fermipy (Wood et al. 2017). This tool has been used in several Fermi-LAT publications (Abeysekara et al. 2018; Ackermann et al. 2018; Di Mauro et al. 2018; Ahnen et al. 2019). It is based on a binned likelihood analysis and, although not optimal for low

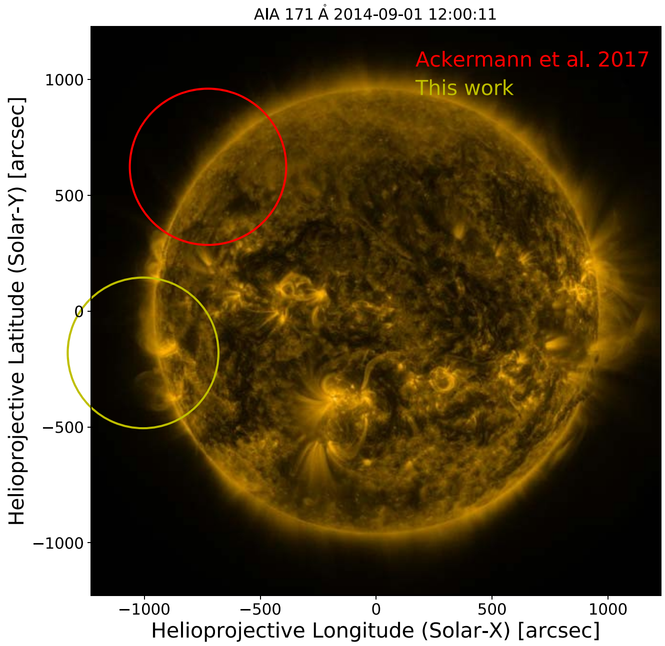

Figure 5. Emission centroid for FLSF 2014 September 1 for energies greater than 100 MeV with a 95% uncertainty error radius using the gttsmap tool and the fish-eye correction in yellow and the previously published position is shown in red (with the 95% uncertainty error radius). The new position is centered at helioprojective coordinates X, Y = [−1105″, −128″] with a 95% uncertainty error radius of 643″.

counting statistics,[65] presents the advantage of being very fast and allows the extension of γ-ray emission to be studied by comparing a model with a source with a radial extension (uniform disk or Gaussian) with the data, and profiling the value of $\log(\mathcal{L})$ by varying the extension radius.

For FLSF 2012 March 7, we use the same time window used in Ajello et al. (2014), namely from 2012 March 7 02:27:00 UT to 2012 March 7 10:14:32 UT, thus avoiding the time interval affected by ACD pile-up. For FLSF 2017 September 10, we use the time window from 2017 September 10 15:56:55 UT to 2017 September 11 02:00:21 UT and SOURCE class events with energies greater than 100 MeV. The RoI is 10° wide. In this analysis the spectra of the FLSFs are described by a power law with exponential cutoff, and the model is reoptimized during the fit procedure. For convenience, we use ThreeML (Vianello et al. 2015) as an interface to fermipy. It allows us to perform the fit to the LAT data using the fermipy plugin, providing, at the same time, an easy interface to download the data and build the model to be fitted. In Figure 6, we show the radial profile of a point-source model compared to the data, for the best-fit model. The model (which is convolved with the IRFs of the instrument), matches very well the radial profile of the counts in both directions, and no residual counts that could suggest the presence of a spatially extended emission are visible. Note that in our analysis we first optimize the localization of the source (hence the offset in Figure 6) and then we test for an extension. The optimized locations are at helioprojective coordinates X, Y = [−400″, 400″] with a 68% uncertainty error radius of 100″ for FLSF 2012 March 7, and X, Y = [600″, −60″] with an uncertainty of 70″ for FLSF 2017 September 10.

Finally, in Figure 7, we show the profile of the likelihood as a function of the radial extension for two different spatial templates, for the two flares. The improvement with respect to the point-source hypothesis is very small (ΔTS < 1.5 in both cases), and only an upper limit of the radius can be placed. The 95% confidence level upper limits (corresponding to a $-\Delta \log(\mathcal{L}) \approx 1.35$) are 0°. 18 for the Gaussian disk and 0°. 14 for the radial disk for FLSF 2012 March 7, and 0°. 23 (Gaussian) and 0°. 17 (radial) for FLSF 2017 September 10. These two events are the only two flares detected by the LAT that are bright enough to allow a dedicated spatial extension analysis. Even so, we can only set an upper limit on the extension that is smaller than the solar radius.

2.6. Total Emission Duration, Fluence, and Total Number of Protons Greater than 500 MeV

With the Sun being observable by the LAT for only 20–40 minutes every 1.5–3 hr, it can be challenging to reconstruct the complete lightcurve and to estimate the true duration of the γ-ray emission. In order to overcome the issues caused by the observational gaps, we are forced to make some assumptions on the behavior of the emission when the Sun is outside of the FoV of the LAT. To identify the start of the FLSF, we rely on the timing of the associated GOES X-ray flare. For example, when the GOES X-ray flare occurs during an LAT data gap and the start of the LAT detection window (t_{start}) occurs after the end of the GOES X-ray flare, we take the end of the GOES X-ray flare as the start of the γ-ray emission. For the cases where the GOES X-ray flare occurs within the detection window and the LAT statistics are not sufficient to perform a fine time binning analysis, we take t_{start} to be the start of the detection window. The end time of the FLSF (t_{stop}) is taken as the midpoint between the end of the last detection window and the start of the following observational window (with an upper limit on the γ-ray emission from the Sun). The total duration of the FLSF is then simply $\Delta t = t_{stop} - t_{start}$. These assumptions on the start and stop of the FLSF are not needed for the short prompt FLSF flares where the true start/stop of the γ-ray emission can be identified within the observational window.

Once we have estimated the start and stop of the FLSF, we can build a functional shape[66] to describe the lightcurve of the FLSF even in the cases where we only have one detection point (see Figure 8). Having a full description of the lightcurve of the FLSF emission, it is possible to evaluate the total γ-ray fluence by simply integrating the lightcurve over the estimated duration of the flare. When integrating, we assume that the flux values at the start and end of the FLSF are equal to 4.6×10^{-7} ph cm^{-2} s^{-1}, which corresponds to the >100 MeV quiet Sun emission.

For every FLSF that is best described by the pion template model, we provide an estimate of N500 needed to produce the γ-ray emission detected in the observational time window. However, if we want to know the total N500 needed to produce the total γ-ray emission over the full duration, then we need to build a functional form (just as was done for the lightcurve) also for the temporal evolution of N500. The start and stop of the FLSF remain the same as described above; the main challenge lies in estimating the value for N500 at t_{start} and t_{stop}. The value of N500 depends on two parameters, the normalization of the spectral function used to fit the data and the best

65 Both FLSF 2012 March 7 and FLSF 2017 September 10 are very bright and a binned likelihood analysis is appropriate.

66 We use scipy splines to build the functional shape of the γ-ray lightcurve.

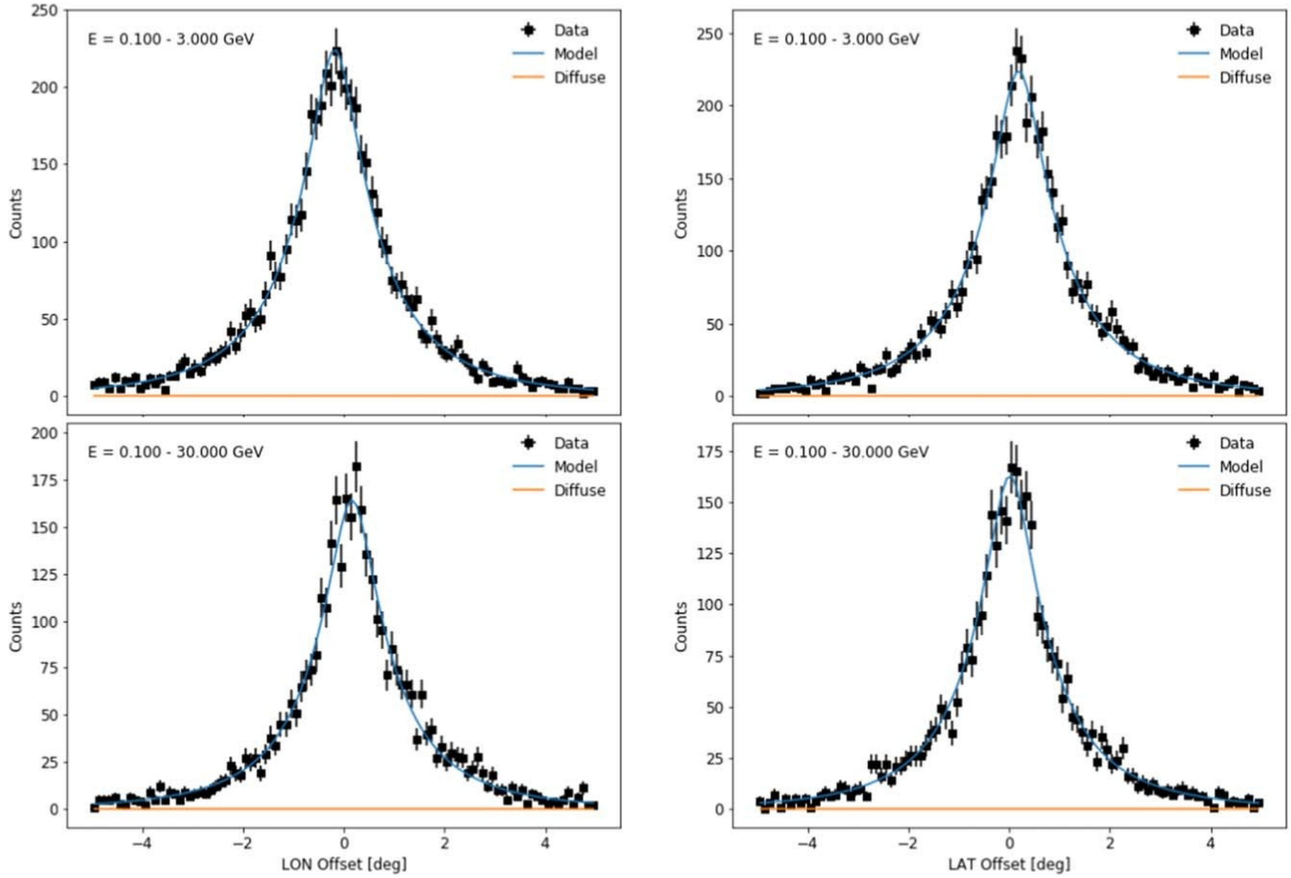

Figure 6. Longitude (left) and latitude (right) radial profile for FLSF 2012 March 7 (top row) and for FLSF 2017 September 10 (bottom row). The x-axis shows the offset with respect to the optimized localization.

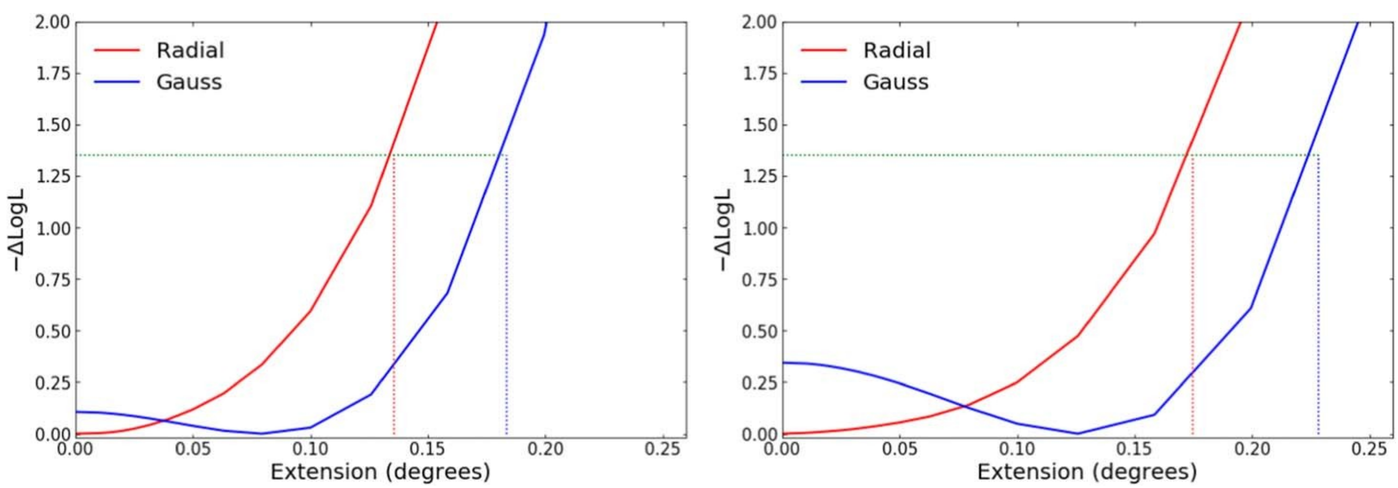

Figure 7. Likelihood profile of FLSF 2012 March 7 (left) and FLSF 2017 September 10 (right) as a function of a spatial profile for a Gaussian profile (Gauss) and a radial profile (Radial). The horizontal green dotted lines show the increment of $-\Delta \log(\mathcal{L}) \approx 1.35$, corresponding to a C.L. of 95%. The blue and red dotted lines are the estimated values for the upper limits on the radius.

proton index resulting from the spectral analysis (as described in 2.3). We therefore find the best value for the N500 corresponding to the quiet Sun flux level by performing a scan over all the possible proton indices (ranging from 2 to 6, with the same gradation as used during the likelihood analysis) and used the average value of 6×10^{22}. Finally, as in the case of the fluence, we integrate the functional form to find the N500 needed to produce the total emission of the FLSF. The values for the total fluence and total N500 with their associated uncertainties for all of the FLSFs in the catalog are listed in Table 1.

The main uncertainties on the fluence and total N500 are due to the values of t_1 and t_2, where t_1 is defined as the duration between the assumed start of the emission (t_{start}) and the start of the detection window and t_2 is the duration between the end of the detection window and the assumed end of the emission

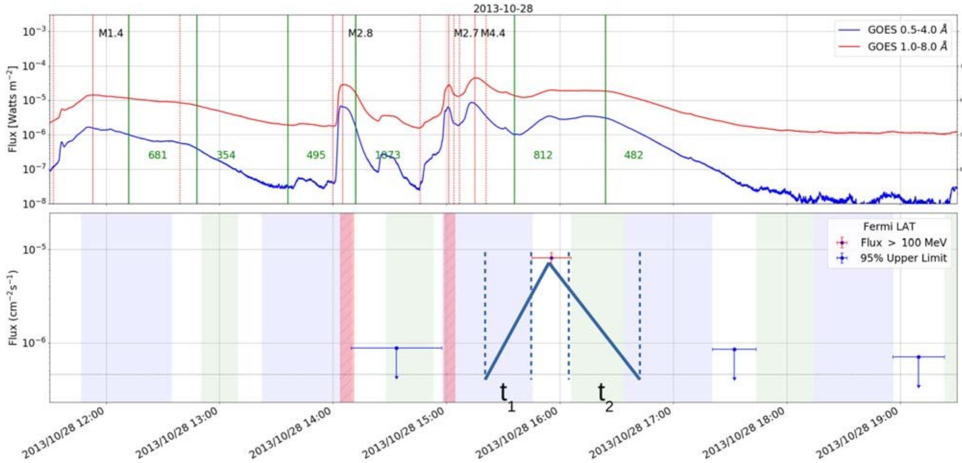

Figure 8. Lightcurve of the >100 MeV emission from FLSF 2013 October 28 with multiple flaring episodes prior to the start of the γ rays. The M2.7 and M4.4 and 812 km s^{-1} CMEs, all from the same active region (AR), are likely associated with the γ-ray emission, although it is possible that the activity from another AR (M2.8 flare and 1073 km s^{-1} CME) may contribute to the γ rays. The solid green lines represent the first appearance of the Large Angle and Spectrometric Coronagraph (LASCO) CME C2; the linear speed value is annotated next to the line (also in green). The dashed/solid red lines represent the start (stop)/peak of the GOES X-ray flare; the GOES class is also annotated next to the solid red line. In the lower panel, the vertical dashed lines denote the t_1 and t_2 quantities, where t_1 is defined as the time between the assumed start of the emission and the start of the detection window and t_2 is the time between the end of the detection window and the assumed end of the emission. For further details on how we use the t_1 and t_2 quantities to determine the uncertainties on the total fluence and total N500, see Section 2.6. The solid triangle represents the assumed lightcurve for this flare. The light-green bands indicate when the Fermi satellite was in the South Atlantic Anomaly (SAA), the blue bands indicate when the Sun was outside of the FoV of the LAT, and the pink bands indicate the presence of potential pile-up in the data.

(t_{stop}). See Figure 8 for an illustration of t_1 and t_2 for the case of the single point detection of FLSF 2013 October 28. To estimate this uncertainty, we vary the value of t_1 and t_2 by ± 50% and repeat the integral over the flux and N500, the error is then found by taking the difference between this value and the nominal one.

3. FLSF Classification

We associate each significant detection of γ-ray emission from solar flares with solar events as seen by other instruments. For most cases, the association of the γ-ray emission to a specific GOES flare or CME is straightforward: linking the FLSF to a single flare or CME within an hour of the start of the γ-rays. In some cases, however, the association with a single GOES flare or a single CME is not obvious when several events happen within a short time frame. In these cases, we tend to pick the GOES flare or the CME closest in time to the γ-ray emission. For example, in the FLSF 2013 October 28 (shown in Figure 8), a series of three M-class flares occurred, accompanied by two CMEs, all prior to the γ-ray detection. In this case, the γ-ray emission is likely associated with the pair of flares M2.7 and M4.4 (both of which started within an hour of the start of the FLSF) from the same AR and the associated CME with speed 812 km s^{-1} (LASCO first appearance occurred ≈ 15 minutes prior to the start of the FLSF).

In the cases of the BTL FLSFs, the soft X-ray emission detected by GOES is either absent or biased toward lower fluxes than would have been the case if it were a disk flare. For those, the STEREO satellites provide the direct extreme ultraviolet (EUV) observation of the flare, which allows us to estimate the peak soft X-ray flux (for a detailed description of this procedure, see Ackermann et al. 2017).

Once we have found a GOES X-ray flare associated with the FLSF, then we can begin to classify the flares in the catalog. In the attempt to better characterize the features present in each of the FLSFs and hopefully to also understand the underlying acceleration mechanisms at work during the flares in the FLSF catalog, we compare the γ-ray timing evolution with that in hard X-Rays. This is because HXR emission traces the high-energy electron population accelerated during the flare energy release and γ-ray signatures of protons accelerated by the same processes and on the same timescales have been observed in the past by SMM and EGRET (Thompson et al. 1993).

The Fermi-GBM (Meegan et al. 2009) on board the Fermi satellite consists of 12 Na sci detectors and two BGO detectors covering the energy range 8 keV–40 MeV. Thanks to the fact that the Fermi-GBM continuously monitors the nonocculted sky, it provides excellent HXR coverage of the FLSFs in this catalog. For each FLSF in the catalog with a time window coincident with the prompt phase of an X-ray solar flare, we compare the HXR evolution observed by the two instruments of the Fermi-GBM to a finely time-resolved γ-ray lightcurve as shown in Figure 9 for the FLSF 2011 September 6. If we find that the γ-ray emission evolution is synchronous with the HXR evolution, we classify it as a prompt flare.

When performing these finely time-resolved lightcurves, different patterns emerge, revealing a more complex picture of the γ-ray solar flares. This can be seen again for FLSF 2011 September 6 (Figure 9). A prompt component coincident with the bright HXR peak appears in γ-rays and is immediately followed by a second phase lasting for more than 20 minutes after the start of the flare. This phase consists of a second, less bright peak with a longer rise and fall timescales, but there is no sign of such behavior in the HXRs. The Sun passed in the FoV two hours later and no γ-rays were detected. Cases such as FLSF 2011 September 6 are classified as prompt short-delayed.

A flare is prompt only if the γ-ray emission does not extend beyond the HXR duration, as was the case for the flare detected on 2010 June 12 (Ackermann et al. 2012b). All flares detected through the LLE method are associated with prompt emission, but some exhibit delayed emission as well. The fine time-resolved lightcurves for all FLSFs classified as prompt are reported at doi:10.5281/zenodo.4311156.

A large number of solar flares observed by Fermi-LAT do not fall in the prompt category: γ-ray emission is detected

Table 1
FLSF Catalog for Flares Detected with the Fermi-LAT SunMonitor and Their Likely GOES X-Ray Flare Associations

Name	GOES Class	GOES Start–Stop	Detection duration (hr)	Total Duration (hr)	Peak Flux (10^{-5}cm^{-2} s^{-1})	Fluence >100 MeV (cm^{-2})	Flare Type
FLSF 2011 Mar 7	M3.7[c]	19:43–20:58	13.5	15.8 ± 3.1	3.23 ± 0.22	1.076 ± 0.029	Delayed
FLSF 2011 Jun 7	M2.5	06:16–06:59	3.8	6.0 ± 2.2	3.18 ± 0.20	0.295 ± 0.030	Delayed
FLSF 2011 Aug 4	M9.3	03:41–04:04	0.7	2.3 ± 0.7	2.30 ± 0.18	0.13 ± 0.05	Delayed
FLSF 2011 Aug 9	X6.9	07:48–08:08	0.5	0.87 ± 0.34	2.29 ± 0.23	0.037 ± 0.018	Prompt Sho
FLSF 2011 Sep 6	X2.1	22:12–22:24	0.6	2.0 ± 1.4	22.8 ± 0.4	0.87 ± 0.17	LLE-Prompt
FLSF 2011 Sep 7	X1.8	22:32–22:44	0.8	2.02 ± 0.35	0.77 ± 0.08	0.041 ± 0.014	Delayed
FLSF 2011 Sep 24	X1.9	09:21–09:48	0.5	1.2 ± 0.7	0.50 ± 0.10	0.014 ± 0.007	LLE-Prompt
FLSF 2012 Jan 23	M8.7	03:38–04:34	5.3	5.9 ± 1.0	1.99 ± 0.12	0.340 ± 0.014	Delayed
FLSF 2012 Jan 27	X1.7	17:37–18:56	5.3	6.8 ± 1.5	3.3 ± 0.5	0.248 ± 0.025	Delayed
FLSF 2012 Mar 5	X1.1	02:30–04:43	3.8	4.4 ± 1.2	0.63 ± 0.07	0.085 ± 0.007	Delayed
FLSF 2012 Mar 7	X5.4[c]	00:02–00:40	19.6	20.3 ± 0.8	233 ± 8	33.996 ± 0.030	Delayed
FLSF 2012 Mar 9	M6.3	03:22–04:18	5.5	7.2 ± 1.7	0.96 ± 0.12	0.148 ± 0.007	No-Prompt D
FLSF 2012 Mar 10	M8.4	17:15–18:30	2.3	6 ± 4	0.23 ± 0.06	0.042 ± 0.012	Delayed
FLSF 2012 May 17	M5.1	01:25–02:14	2.1	2.6 ± 0.5	1.19 ± 0.19	0.0572 ± 0.0026	Delayed
FLSF 2012 Jun 3	M3.3	17:48–17:57	0.4	1.9 ± 1.5	3.06 ± 0.25	0.117 ± 0.031	LLE-Prompt
FLSF 2012 Jul 6	X1.1	23:01–23:14	0.8	1.27 ± 0.35	3.06 ± 0.15	0.100 ± 0.021	Delayed
FLSF 2012 Oct 23	X1.8	03:13–03:21	0.5	1.9 ± 0.5	0.73 ± 0.18	0.047 ± 0.018	LLE-Prompt
FLSF 2012 Nov 13	M6.0	01:58–02:04	0.7	0.041 ± 0.006	0.46 ± 0.09	0.006 ± 0.022	Prompt
FLSF 2012 Nov 27	M1.6	15:52–16:03	0.8	0.166 ± 0.025	0.27 ± 0.07	0.005 ± 0.030	Prompt Sho
FLSF 2013 Apr 11	M6.5	06:55–07:29	0.7	0.38 ± 0.27	5.71 ± 0.24	0.099 ± 0.016	No-Prompt S
FLSF 2013 May 13a	X1.7	01:53–02:32	0.7	4.0 ± 1.3	0.96 ± 0.11	0.11 ± 0.06	Delayed
FLSF 2013 May 13b	X2.8	15:48–16:16	3.9	6.1 ± 2.2	2.41 ± 0.21	0.35 ± 0.04	Delayed
FLSF 2013 May 14	X3.2	00:00–01:20	5.6	5.9 ± 0.5	3.30 ± 0.15	0.401 ± 0.004	No-Prompt D
FLSF 2013 May 15	X1.2	01:25–01:58	0.8	3.5 ± 0.5	0.36 ± 0.07	0.052 ± 0.023	No-Prompt D
FLSF 2013 Oct 11	M4.9*	07:01–07:45	0.7	0.38 ± 0.32	12.5 ± 0.4	0.262 ± 0.013	BTL Short-D
FLSF 2013 Oct 25a	X1.7	07:53–08:09	0.7	1.4 ± 0.5	1.15 ± 0.12	0.042 ± 0.013	Delayed
FLSF 2013 Oct 28 c	M2.7[c]	14:46–15:04	0.3	1.6 ± 0.6	0.81 ± 0.12	0.036 ± 0.014	Delayed
FLSF 2014 Jan 06	X3.5*	07:40–08:08	0.6	0.27 ± 0.04	0.42 ± 0.09	0.0061 ± 0.0028	BTL Short-D
FLSF 2014 Jan 07	X1.2	18:04–18:58	0.8	1.05 ± 0.26	0.29 ± 0.07	0.0081 ± 0.0020	Delayed
FLSF 2014 February 25	X4.9	00:39–01:03	6.7	8.4 ± 1.8	169.6 ± 2.0	13.95 ± 0.18	LLE-Prompt
FLSF 2014 Jun 10	X1.5	12:36–13:03	0.4	1.9 ± 0.6	1.17 ± 0.26	0.064 ± 0.026	LLE-Prompt
FLSF 2014 Jun 11	X1.0	08:59–09:10	0.4	0.23 ± 0.17	0.99 ± 0.26	0.007 ± 0.005	Short-Delay
FLSF 2014 Sep 1	X2.4*	10:58–11:40	1.9	2.5 ± 1.2	379 ± 7	12.1 ± 2.3	BTL Delaye
FLSF 2014 Sep 10	X1.6	17:21–18:20	0.3	0.30 ± 0.06	7.4 ± 0.5	0.172 ± 0.012	Short-Delay
FLSF 2015 Jun 21	M2.7[c]	02:04–03:15	10.1	11.5 ± 2.5	1.26 ± 0.15	0.296 ± 0.011	Prompt Dela
FLSF 2015 Jun 25	M7.9	08:02–09:05	0.7	2.4 ± 1.3	0.40 ± 0.08	0.030 ± 0.004	Delayed
FLSF 2017 Sep 6a	X2.2	08:57–09:17	0.5	0.169 ± 0.025	1.31 ± 0.16	0.020 ± 0.007	Prompt
FLSF 2017 Sep 6b	X9.3[c]	11:53–12:10	13.0	13.33 ± 0.32	3.6 ± 0.5	1.0700 ± 0.0022	Delayed
FLSF 2017 Sep 10	X8.2	15:35–16:31	13.3	13.9 ± 1.2	291.0 ± 2.1	22.2 ± 1.6	Prompt Dela

Note. In the GOES-class column, entries with * identify the BTL flares, whose class is estimated based on the STEREO observation, and [c] indicates that there is also an L
for the LLE flares are shown in Table 3.

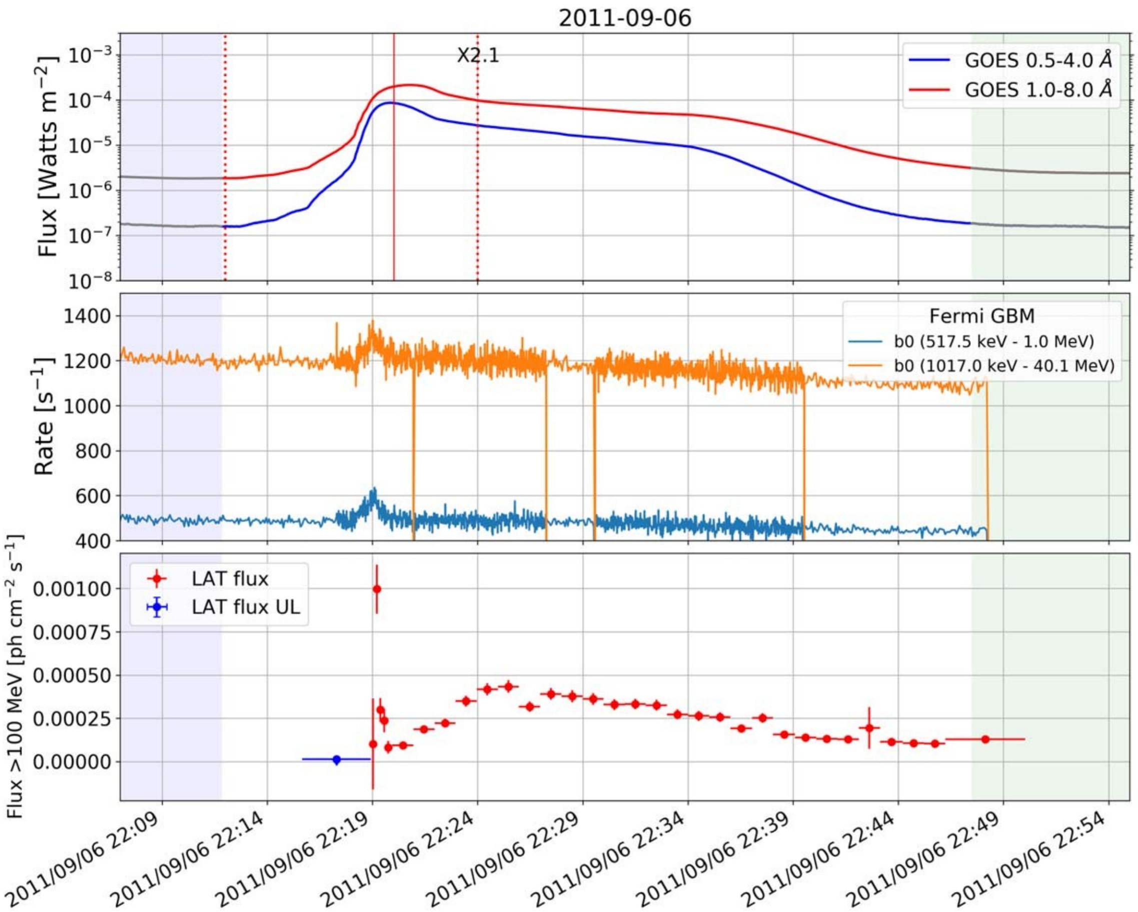

Figure 9. Example of a flare with a prompt component coincident with the bright HXR peak followed by a γ-ray delayed emission; that occurred on 2011 September 6. From top to bottom, the GOES X-ray flux in two energy bands, the Fermi-GBM X-ray lightcurve, and the Fermi-LAT >100 MeV flux using the standard likelihood analysis with a fine time binning to reveal the prompt component. The dashed/solid red lines represent the start (stop)/peak of the GOES X-ray flare; the GOES class is also annotated next to the solid red line.

beyond the end of the HXR emission and even the end of the SXR seen by GOES. We refer to that general category as delayed emission. The subset of flares classified as delayed also exhibit a wide variety of behaviors. For example, there are cases where no significant γ-rays are detected during the prompt phase of the flare in X-rays, but γ-ray emission seen rising and falling later on. We refer to these flares as being delayed only.

One of the most interesting results of the Fermi-LAT observations of solar flares is events with detectable emission lasting several hours. As already discussed in Section 1, the LAT has the Sun in its FoV on average only 40% of its orbit, greatly limiting the coverage of these delayed γ-ray flares. As a result, it is difficult to study the time profiles of these flares throughout the entire duration of the emission.

This is the case for the FLSF 2012 March 9, which is associated with a GOES M6.3 flare with HXR extending up to the GBM Na sci 100–300 KeV channel. Most of the prompt phase was observable by the Fermi-LAT and the bright SXR affected the instrument response (BTI in red in Figure 10). No γ-ray emission was detected during the peak of the prompt phase using the S15 event class or the LLE analysis method. Yet γ-ray emission was detected when the Sun came back in the FoV, almost two hours after the start of the flare in X-rays, and lasted for four orbits. It followed a rise and fall pattern, reaching its peak after 4 hr and ending 7 hr after the start of the flare in X-rays.

Similarly, the FLSF 2013 May 15 had no significant emission detected during either the impulsive phase or in the first time window following the flare, but significant emission detected in the following time window (Figure 11). In itself, it might not be a new type of behavior, as it can be seen as a rise-and-fall pattern with the starting flux being just below the Fermi-LAT sensitivity but the peak flux being high enough to be detected.

These behaviors highlight the possibility that high-energy emission above 100 MeV can arise at later times, even if the prompt phase itself did not show a strong nonthermal component (almost no HXR above 300 keV and no γ-rays below 30 MeV). Although these cases are rare (only four cases in the catalog), they are particularly interesting for understanding whether the acceleration of high-energy particles is solely due to the prompt phase of solar flares or due to a separate mechanism entirely.

There are also FLSFs with both a clear prompt and a long-duration delayed component present; these flares are classified as prompt-delayed. An example of this class of flares is the FLSF 2017 September 10 (Omodei et al. 2018) that exhibited a very bright prompt phase and almost 14 hr of delayed γ-ray emission. In the FLSF catalog, we were able to classify the flares into six different categories: prompt, prompt only,

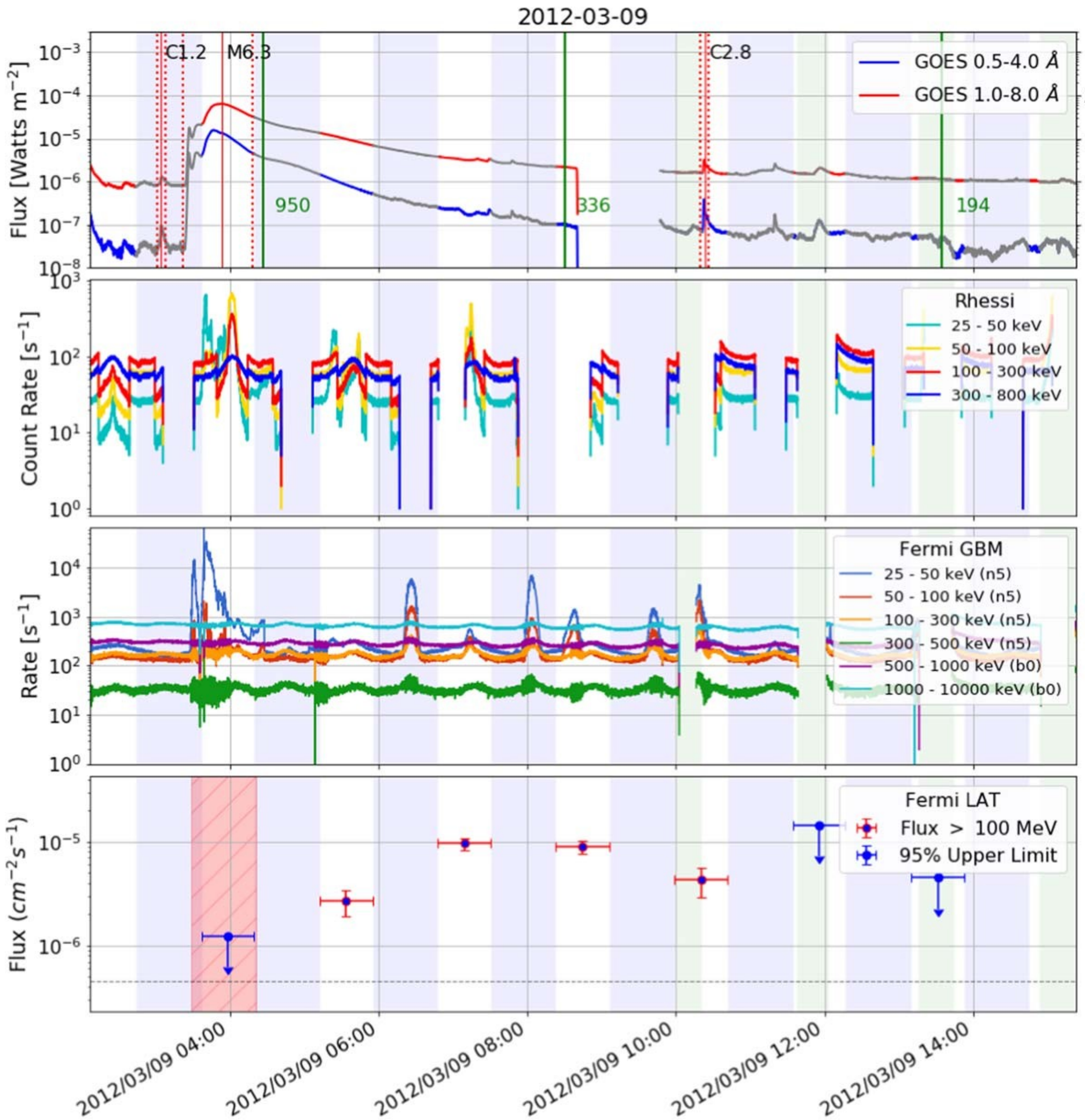

Figure 10. Lightcurve of the >100 MeV emission from FLSF 2012 March 9 lasting more than 6 hr but with no detectable high-energy γ-ray emission in the impulsiv phase, classified as delayed only. The four panels report the lightcurve measured by GOES, RHESSI, Fermi/GBM, and Fermi/LAT in various energy ranges. The solid green lines represent the first appearance of the LASCO CME C2; the linear speed value is annotated next to the line (also in green). The dashed/solid red li represent the start (stop)/peak of the GOES X-ray flare; the GOES class is also annotated next to the solid red line. The light-green bands indicate when the Fermi satellite was in the SAA, and the blue bands indicate when the Sun was outside of the FoV of the LAT. The pink bands indicate the time interval over which potenti pile-up effects could be present.

delayed, delayed only, prompt short-delayed, prompt-delayed. All of the lightcurves and categories of FLSFs are reported at doi:10.5281/zenodo.4311156.

4. Results

Continuous monitoring of the Sun has led to the high-confidence (TS 30) detection of 45 solar flares with γ-ray emission above 60 MeV. For 39 of these flares, γ-ray emission was significant in 92 SunMonitor time windows. The remaining six flares were detected with LLE analysis only. Of these 45 flares, 6 are classified as prompt only, 4 are classified as delayed only, and for 10 flares both the prompt and delayed emission were clearly observed by Fermi-LAT. For the remaining cases, we cannot exclude the presence of a prompt emission because the Sun was not in the FoV of the LAT during the HXR activity. Because of the observing strategy of the Fermi-LAT, more than half of the solar flares detected are only detected in a single time window, whereas 16 are detected in more than one window. Of the 16 flares detected in multiple time windows, 5 are detected in only 2 time windows, and 11 are detected in 3 or more (up to 11) time windows well beyond the HXR signatures of the high-energy electrons. Seven flares in the latter group show a well-defined pattern of rise and decay phases after the end of the HXR and 2 show a decay phase only. All five flares detected in two time windows show a decay between the two points. Some of these may represent a rise and fa case with a peak occurring in between the two time windows. However, this is unlikely because statistically, one would expect two or three of these flares showing rise instead of decay, and because this would imply a faster rise and fall than seen in the flares with more than three windows of observation.

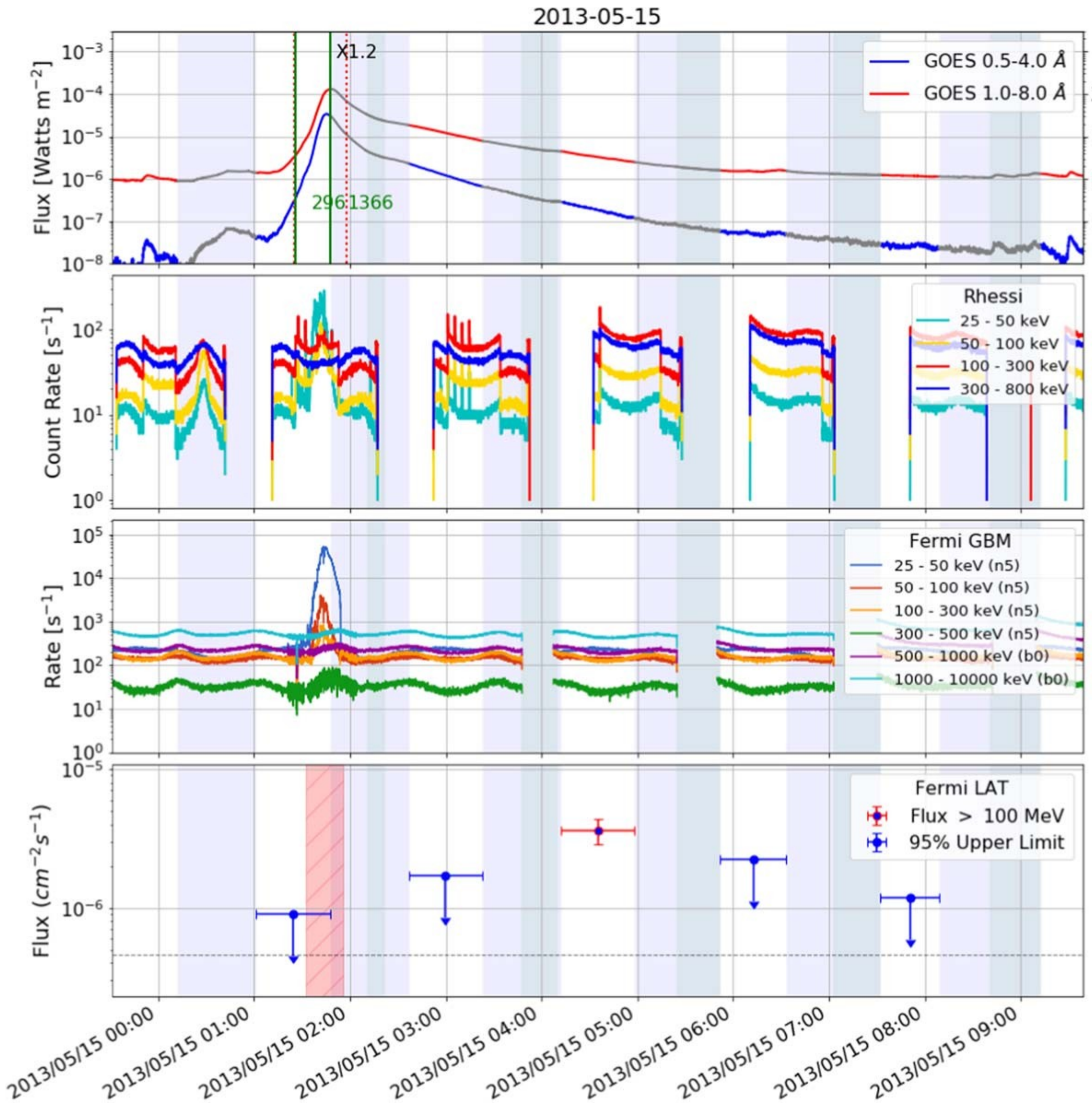

Figure 11. The delayed-only lightcurve of the >100 MeV emission from the FLSF 2013 May 15 flare with no detectable high-energy γ-ray emission in the impulsive phase or the following time window. The four panels report the same quantities as those in Figure 10.

In Table 1, we show the time-integrated results for the FLSFs detected with the SunMonitor. The columns report the LAT detection start date and time, the GOES soft X-ray start and end times, the LAT detection duration, the total duration of the FLSF,[67] the fluence, namely the time-integrated flux over the total duration, the FLSF flare type, and the total number of accelerated >500 MeV protons (N500). The GOES classes for the three BTL flares (identified by an *) are estimated based on STEREO UV fluxes as described in Pesce-Rollins et al. (2015).

The characteristics of the γ-ray emission in each SunMonitor time window are listed in Table 2. Results from flares detected in more than one time window are listed together. The columns of Table 2 are the time of each detection window, the duration of the window, the >100 MeV flux, TS, and the spectral parameters (power-law indices and cutoff energies) of the best-fitting photon model. For the cases where the ΔTS > 9, we give the proton index based on the pion-decay model in the last column. The fluxes are given in 10^{-5} ph cm^{-2} s^{-1} and calculated for the emission between 100 MeV and 10 GeV. The LAT emission in all SunMonitor time windows with TS larger than 70 shows significant spectral curvature and can be well described with the exponential cutoff model. This does not mean that all fainter γ-ray flares are only consistent with a power-law model, but rather that the lower statistics make it impossible to distinguish between the two.[68]

We retract the LAT detection of the C-class flare on 2011 June 2 reported in Ackermann et al. (2014), because during the month of June, the Sun passes through the Galactic plane, and a higher background flux of photons enters into the RoI around the Sun relative to other periods in the year. After careful reanalysis of this event, we found that the reported detection was not statistically significant.

[67] The detection duration is simply the sum of the SunMonitor detection windows duration while the total duration is that found using the approach described in Section 2.6.

[68] The FLSF of 2013 October 28 is the only exception, having a TS of 120 and the exponential cutoff model is not preferred (ΔTS = 8).

Table 2
Maximum Likelihood Results for Each SunMonitor Observing Time Window Associated with a Solar Flare Detected by the Fermi-LAT

Date and Time (UTC)	Exposure (minutes)	Flux (10^{-5} ph cm^{-2} s^{-1})	TS	ΔTS	Model	Photon Index	Cutoff Energy (MeV)	Proton index
2011 Mar 7 20:10–20:39	29	2.06 ± 0.19	317	27	Exp	−0.76 ± 0.45	172 ± 55	4.3 ± 0.4
2011 Mar 7 23:21–00:05	44	3.04 ± 0.20	710	70	Exp	−0.31 ± 0.36	138 ± 27	4.13 ± 0.26
2011 Mar 8 02:33–03:16	43	3.23 ± 0.22	621	66	Exp	−0.15 ± 0.41	110 ± 22	4.70 ± 0.32
2011 Mar 8 05:44–06:27	44	1.40 ± 0.15	219	32	Exp	0.67 ± 0.99	63 ± 22	>6
2011 Mar 8 09:13–09:39	26	0.48 ± 0.11	46	−0.1	PL	−2.55 ± 0.25	L	L
2011 Jun 7 07:47–08:23	36	3.18 ± 0.20	740	76	Exp	−0.13 ± 0.37	104 ± 19	4.97 ± 0.33
2011 Jun 7 11:16–11:34	19	0.32 ± 0.10	19	5	PL	−2.70 ± 0.35	L	L
2011 Aug 4 04:55–05:37	42	2.30 ± 0.18	413	49	Exp	−0.09 ± 0.50	95 ± 21	5.4 ± 0.4
2011 Aug 9 07:37–08:09	32	2.29 ± 0.23*	186	26	Exp	−0.04 ± 0.87	91 ± 37	5.4 ± 0.6
2011 Sep 6 22:11–22:47	36	22.8 ± 0.4*	8197	437	Exp	−0.89 ± 0.09	161 ± 11	4.89 ± 0.11
2011 Sep 7 23:35–00:23	48	0.77 ± 0.08	270	30	Exp	−0.10 ± 0.69	114 ± 40	4.4 ± 0.5
2011 Sep 24 09:18–09:47	30	0.50 ± 0.10*	50	5	PL	−2.51 ± 0.22	L	L
2012 Jan 23 04:06–04:46	40	1.12 ± 0.11	258	26	Exp	0.12 ± 1.09	81 ± 40	5.5 ± 0.6
2012 Jan 23 05:33–06:21	48	1.99 ± 0.12	796	92	Exp	0.25 ± 0.41	80 ± 13	5.6 ± 0.4
2012 Jan 23 07:20–07:47	27	1.97 ± 0.31	93	12	Exp	−0.25 ± 1.05	100 ± 49	5.5 ± 0.9
2012 Jan 23 08:58–09:26	28	1.63 ± 0.23	116	27	Exp	1.81 ± 1.41	51 ± 18	5.6 ± 0.8
2012 Jan 27 19:37–19:55	18	3.3 ± 0.5	102	14	Exp	0.31 ± 1.43	65 ± 33	>6
2012 Jan 27 21:08–21:36	28	0.72 ± 0.14	66	8	PL	−2.53 ± 0.20	L	L
2012 Jan 28 00:19–00:55	36	0.25 ± 0.09	19	1	PL	−2.60 ± 0.39	L	L
2012 Mar 5 04:07–04:49	42	0.58 ± 0.09	100	11	Exp	0.34 ± 1.33	63 ± 31	>6
2012 Mar 5 05:36–06:24	48	0.63 ± 0.07	175	16	Exp	−0.20 ± 0.85	79 ± 31	>6
2012 Mar 5 07:18–07:54	36	0.55 ± 0.11	53	6	PL	−2.52 ± 0.21	L	L
2012 Mar 7 00:40–01:20	40	233 ± 8*	75611	−254574	Exp	−0.65 ± 0.03	182 ± 4	3.875 ± 0.025
2012 Mar 7 02:26–02:45	18	75.1 ± 2.6	2377	117	Exp	−1.45 ± 0.13	355 ± 47	3.77 ± 0.10
2012 Mar 7 03:51–04:31	40	95.1 ± 1.2	21100	1459	Exp	−0.84 ± 0.05	199 ± 8	4.01 ± 0.05
2012 Mar 7 05:38–05:55	18	97.3 ± 3.2	2675	249	Exp	−0.59 ± 0.17	147 ± 14	4.51 ± 0.13
2012 Mar 7 07:02–07:42	40	62.8 ± 1.0	12829	1210	Exp	−0.30 ± 0.08	120 ± 5	4.71 ± 0.07
2012 Mar 7 08:49–09:06	17	49.8 ± 2.5	1181	123	Exp	−0.17 ± 0.32	102 ± 14	5.17 ± 0.24
2012 Mar 7 10:14–10:54	25	26.8 ± 0.9	2803	344	Exp	0.27 ± 0.21	84 ± 7	5.28 ± 0.17
2012 Mar 7 13:24–14:04	13	8.6 ± 0.9	258	31	Exp	0.30 ± 0.75	78 ± 22	5.7 ± 0.6
2012 Mar 7 16:35–16:48	13	1.54± 0.32	49	10	Exp	1.41 ± 1.91	46 ± 23	>6
2012 Mar 7 18:23–18:32	9	2.2 ± 0.7	25	8	PL	−2.91 ± 0.41	L	L
2012 Mar 7 19:46–20:15	29	0.26 ± 0.08	22	3	PL	−2.37 ± 0.30	L	L
2012 Mar 9 05:12–05:55	43	0.27 ± 0.08	32	−0.2	PL	−2.24 ± 0.25	L	L
2012 Mar 9 06:47–07:30	43	0.96 ± 0.12	139	20	Exp	0.09 ± 0.92	87 ± 34	5.5 ± 0.7
2012 Mar 9 08:22–09:05	43	0.89 ± 0.12	140	28	Exp	1.78 ± 1.21	50 ± 15	5.6 ± 0.8
2012 Mar 9 09:58–10:41	22	0.43 ± 0.13	25	0.3	PL	−2.51 ± 0.32	L	L
2012 Mar 10 21:00–21:34	34	0.23 ± 0.06	25	2	PL	−2.50 ± 0.30	L	L
2012 Mar 10 22:35–23:15	40	0.19 ± 0.06	18	3	PL	−3.04 ± 0.40	L	L
2012 May 17 02:12–02:44	32	1.19 ± 0.19	100	10	Exp	−0.72 ± 0.77	207 ± 117	3.7 ± 0.5
2012 May 17 03:49–04:18	30	0.44 ± 0.13	29	7	PL	−2.30 ± 0.28	L	L
2012 Jun 3 17:38–18:02	24	3.06 ± 0.25	395	39	Exp	−0.19 ± 0.63	104 ± 34	5.0 ± 0.4
2012 Jul 6 23:20–00:08	48	3.06 ± 0.15	1173	143	Exp	0.40 ± 0.35	74 ± 10	5.75 ± 0.29
2012 Oct 23 04:13–04:43	30	0.73 ± 0.18	39	9	PL	−2.73 ± 0.27	L	L
2012 Nov 13 01:34–02:14	40	0.46 ± 0.09*	60	7	PL	−2.61 ± 0.21	L	L
2012 Nov 27 15:48–16:34	46	0.27 ± 0.07	44	2	PL	−2.22 ± 0.21	L	L
2013 Apr 11 07:00–07:39	39	5.71 ± 0.24*	1422	120	Exp	−0.43 ± 0.27	105 ± 15	5.67 ± 0.27
2013 May 13 17:15–17:58	30	2.41 ± 0.21	371	43	Exp	−0.24 ± 0.48	142 ± 38	3.91 ± 0.31
2013 May 13 20:26–21:09	43	1.72 ± 0.14	371	43	Exp	0.21 ± 0.73	80 ± 25	5.5 ± 0.5

Table 2
(Continued)

Date and Time (UTC)	Exposure (minutes)	Flux (10^{-5} ph cm^{-2} s^{-1})	TS	ΔTS	Model	Photon Index	Cutoff Energy (MeV)	Proton index
2013 May 13 04:31–05:14	43	0.96 ± 0.11	188	36	Exp	3.00 ± 0.14	31 ± 2	>6
2013 May 14 01:08–01:55	47	1.02 ± 0.09*	292	46	Exp	0.55 ± 0.67	65 ± 15	>6
2013 May 14 02:43–03:31	47	3.30 ± 0.15	1518	193	Exp	0.62 ± 0.32	77 ± 9	4.95 ± 0.24
2013 May 14 04:19–05:06	47	2.32 ± 0.16	546	87	Exp	1.26 ± 0.61	54 ± 9	5.9 ± 0.4
2013 May 14 05:59–06:42	42	0.59 ± 0.09	105	19	Exp	1.05 ± 1.43	54 ± 24	>6
2013 May 15 04:12–04:58	46	0.36 ± 0.07	51	9	PL	−2.62 ± 0.22	L	L
2013 Oct 11 06:56–07:39	42	12.5 ± 0.4	3949	317	Exp	−0.34 ± 0.16	131 ± 12	4.33 ± 0.12
2013 Oct 25 08:15–08:57	42	1.15 ± 0.12*	211	21	Exp	0.07 ± 0.88	79 ± 30	6 ± 4
2013 Oct 28 15:45–16:05	21	0.81 ± 0.12	120	8	PL	−2.32 ± 0.15	L	L
2014 Jan 06 07:55–08:30	34	0.42 ± 0.09	52	13	Exp	1.84 ± 2.16	49 ± 26	5.8 ± 1.9
2014 Jan 07 18:41–19:29	48	0.29 ± 0.07	32	5	PL	−2.68 ± 0.27	L	L
2014 Feb 25 01:09–01:29	20	169.6 ± 2.0*	24030	2121	Exp	−0.33 ± 0.06	154 ± 5	3.78 ± 0.04
2014 Feb 25 04:20–04:40	20	28.3 ± 0.9	2707	370	Exp	1.17 ± 0.28	47 ± 4	>6
2014 Feb 25 07:30–07:51	21	0.87 ± 0.17	74	11	Exp	2.39 ± 2.53	29 ± 14	>6
2014 Jun 10 14:00–14:26	25	1.17 ± 0.26	49	5	PL	−2.47 ± 0.22	L	L
2014 Jun 11 09:06–09:30	24	0.99 ± 0.26*	30	3	PL	−2.77 ± 0.30	L	L
2014 Sep 1 11:02–11:18	16	379 ± 7	41620	−5590	Exp	−1.03 ± 0.09	177 ± 10	4.70 ± 0.07
2014 Sep 1 12:25–12:57	32	2.98 ± 0.22	545	31	Exp	−1.16 ± 0.29	290 ± 82	3.72 ± 0.24
2014 Sep 10 17:35–17:53	18	7.4 ± 0.5*	559	66	Exp	0.35 ± 0.54	86 ± 20	4.66 ± 0.34
2015 Jun 21 02:09–02:42	33	0.25 ± 0.08	23	5	PL	−3.05 ± 0.39	L	L
2015 Jun 21 05:19–05:53	33	1.26 ± 0.15	162	16	Exp	−0.18 ± 0.74	118 ± 44	4.3 ± 0.6
2015 Jun 21 08:30–09:03	33	0.81 ± 0.13	101	12	Exp	0.03 ± 1.14	110 ± 57	4.2 ± 0.7
2015 Jun 21 11:40–12:14	33	0.38 ± 0.10	31	10	Exp	2.05 ± 2.61	49 ± 29	>6
2015 Jun 25 09:24–10:09	45	0.40 ± 0.08	48	6	PL	−2.72 ± 0.22	L	L
2017 Sep 6 12:10–12:35	25	0.96 ± 0.11*	156	17	Exp	0.05 ± 1.06	58 ± 23	>6
2017 Sep 6 13:23–14:10	26	2.63 ± 0.17*	604	66	Exp	0.39 ± 0.55	60 ± 12	>6
2017 Sep 6 15:03–15:40	18	2.9 ± 0.4	137	24	Exp	1.20 ± 1.29	59 ± 23	5.6 ± 0.8
2017 Sep 6 16:45–17:09	19	3.6 ± 0.5	130	24	Exp	1.24 ± 1.24	64 ± 22	5.2 ± 0.7
2017 Sep 6 18:14–18:50	36	2.73 ± 0.24	337	49	Exp	0.67 ± 0.68	71 ± 17	5.4 ± 0.5
2017 Sep 6 19:55–20:20	25	2.27 ± 0.35	96	17	Exp	0.74 ± 1.33	65 ± 27	>6
2017 Sep 6 21:25–22:00	35	2.56 ± 0.24	318	36	Exp	0.11 ± 0.67	84 ± 24	5.5 ± 0.5
2017 Sep 6 23:05–23:31	26	0.96 ± 0.22	43	4	PL	−3.06 ± 0.30	L	L
2017 Sep 7 00:36–01:11	35	0.62 ± 0.13	52	4	PL	−2.63 ± 0.22	L	L
2017 Sep 6 08:51–09:19	28	1.31 ± 0.16*	130	21	Exp	0.59 ± 1.05	60 ± 22	>6
2017 Sep 10 15:52–16:28	35	291.0 ± 2.1*	61725	4429	Exp	−0.67 ± 0.03	195 ± 4	3.737 ± 0.026
2017 Sep 10 17:33–17:58	24	76.4 ± 1.9	6112	469	Exp	−0.70 ± 0.30	248 ± 49	3.30 ± 0.06
2017 Sep 10 19:03–19:39	36	88.3 ± 1.3	16954	1819	Exp	−0.02 ± 0.07	140 ± 5	3.70 ± 0.05
2017 Sep 10 20:44–21:08	24	35.8 ± 1.3	2311	276	Exp	0.07 ± 0.22	117 ± 11	4.18 ± 0.14
2017 Sep 10 22:13–22:49	36	15.0 ± 0.5	2559	315	Exp	0.35 ± 0.22	91 ± 8	4.67 ± 0.16
2017 Sep 10 23:54–00:18	24	5.6 ± 0.5	310	68	Exp	2.03 ± 0.84	55 ± 11	4.9 ± 0.4
2017 Sep 11 01:23–02:00	36	2.38 ± 0.22	284	55	Exp	1.69 ± 0.83	48 ± 10	6.0 ± 0.5
2017 Sep 11 03:05–03:29	24	1.39 ± 0.28	59	12	Exp	1.00 ± 1.58	70 ± 34	5.0 ± 1.0
2017 Sep 11 04:34–05:11	37	0.49 ± 0.11	43	2	PL	−2.65 ± 0.24	L	L

Note. Some flares are detected in more than one time window. The horizontal lines separate the flares. The columns are the start date and time of the observing window (reported in UTC), the exposure of the time window, the flux >100 MeV integrated over the observing time window, the TS value for the simple power-law model fit, the ΔTS between the power-law and the power-law with exponential cutoff fit, the model with higher TS value, the photon index from the best-fit model, the cutoff energy value (for the cases where the exponential cutoff model best fits the data), best proton index (from fit to the data with pion templates) for the case where the curved model best describes the data.

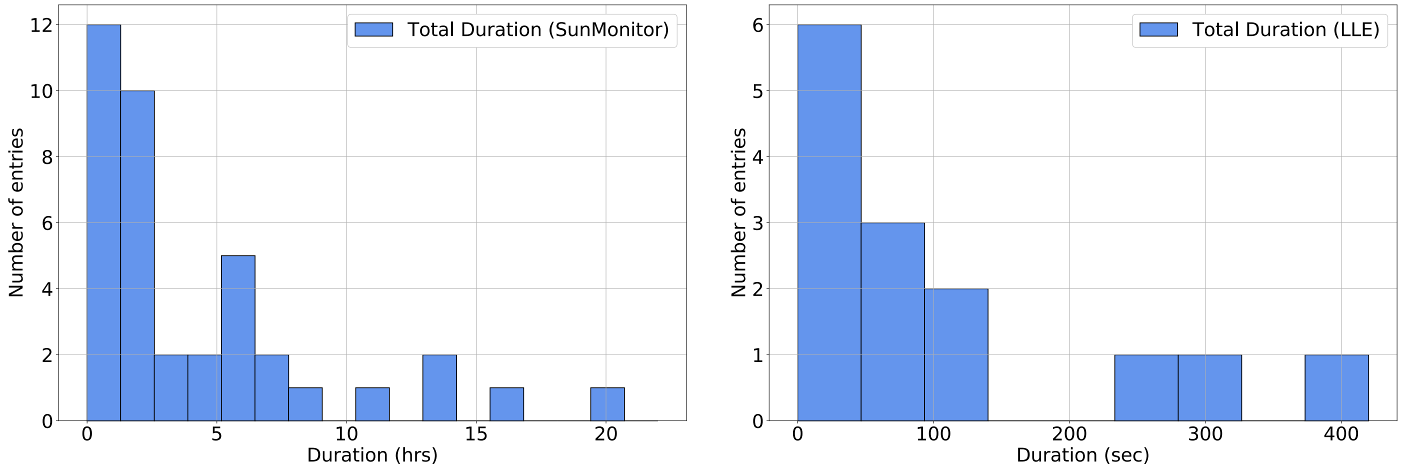

Figure 12. Distribution of the total duration for all of the SunMonitor detected flares (in hours, left panel) and the LLE detected flares (in seconds, right panel) in the FLSF catalog.

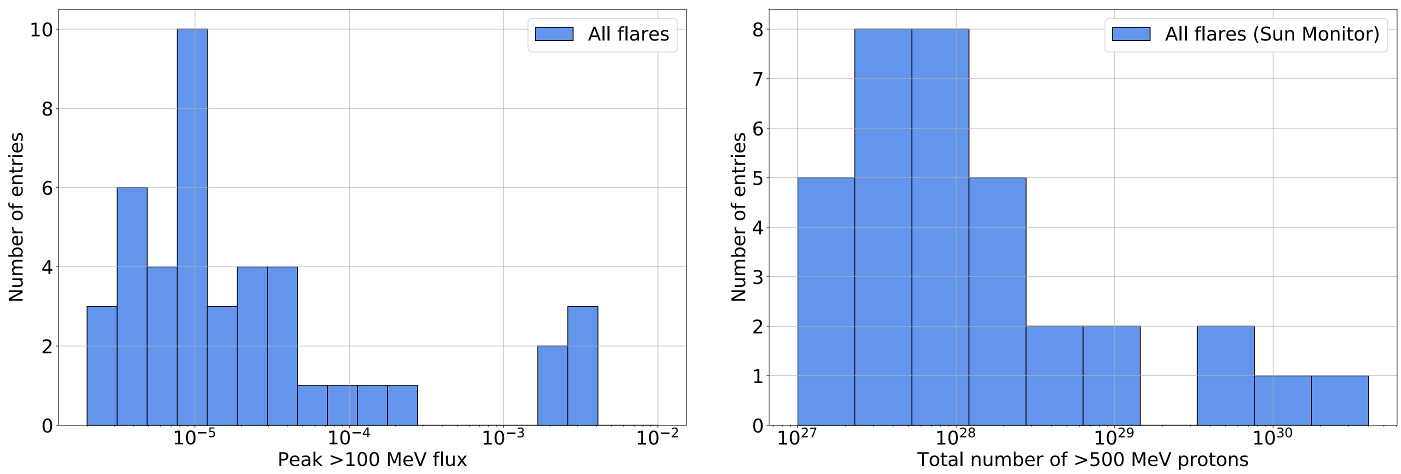

Figure 13. Distributions of the peak >100 MeV flux (in ph cm^{-2} s^{-1}; left panel) for all FLSFs in the catalog and the total number of accelerated >500 MeV protons needed to produce the detected γ-ray emission for each of the SunMonitor detected FLSFs (right panel).

Table 3
LLE FLSF Catalog Results with Associated GOES X-Ray Flare

Name	Start (UTC)	Duration (s)	Flux (30 MeV–10 GeV)	Flux (100 MeV–10 GeV)	Proton Index	GOES Class	SunMonitor Detected
FLSF 2010 Jun 12	2010 Jun 12 00:55:49	30	446 ± 35	191 ± 12	6.0 ± 0.4	M2.0	NO
FLSF 2011 Aug 9	2011 Aug 9 08:01:51	250	31.20 ± 0.24	13.02 ± 0.22	5.68 ± 0.13	X6.9	YES
FLSF 2011 Sep 6	2011 Sep 6 22:18:07	100	54.0 ± 1.4	16.6 ± 1.1	3.2 ± 0.4	X2.1	YES
FLSF 2011 Sep 24	2011 Sep 24 09:35:53	100	65.2 ± 1.7	0.43 ± 0.07	3.2 ± 0.4	X1.9	YES
FLSF 2012 Jun 3	2012 Jun 3 17:53:20	20	111 ± 5	50 ± 5	6.0 ± 1.5	M3.3	YES
FLSF 2012 Aug 6	2012 Aug 6 04:36:01	30	205 ± 5	1.79 ± 0.12	6.0 ± 1.5	M1.6	NO
FLSF 2012 Oct 23	2012 Oct 23 03:15:33	20	$(3.08 \pm 0.27) \times 10^3$	105 ± 20	6.0 ± 1.5	X1.8	YES
FLSF 2013 Oct 25b	2013 Oct 25 20:56:52	10	38.9 ± 1.0	1.13 ± 0.09	6.0 ± 1.5	M1.9	NO
FLSF 2013 Oct 28a	2013 Oct 28 01:59:15	70	0.450 ± 0.035	$<3 \times 10^{-3}$	6.0 ± 1.5	X1.0	NO
FLSF 2013 Oct 28b	2013 Oct 28 04:37:48	50	25.9 ± 1.3	0.0029 ± 0.0016	6.0 ± 1.5	M5.1	NO
FLSF 2013 Oct 28d	2013 Oct 28 20:54:47	50	9.8 ± 0.6	0.33 ± 0.05	6.0 ± 1.5	M1.5	NO
FLSF 2014 Feb 25	2014 Feb 25 00:44:47	400	1407 ± 25	631 ± 26	6.0 ± 0.7	X4.9	YES
FLSF 2014 Jun 10	2014 Jun 10 12:47:18	25	6.7 ± 1.3	2.9 ± 1.1	2.2 ± 1.4	X1.5	YES
FLSF 2017 Sep 10	2017 Sep 10 15:57:47	325	1060 ± 9	601 ± 7	3.01 ± 0.04	X8.2	YES

Note. For the cases where the curved spectrum is preferred, we also list the best inferred proton index. The SunMonitor detected column indicates whether the flare was detected by the SunMonitor automatic pipeline. The fluxes are in units of 10^{-5} ph s^{-1} cm^{-2}.

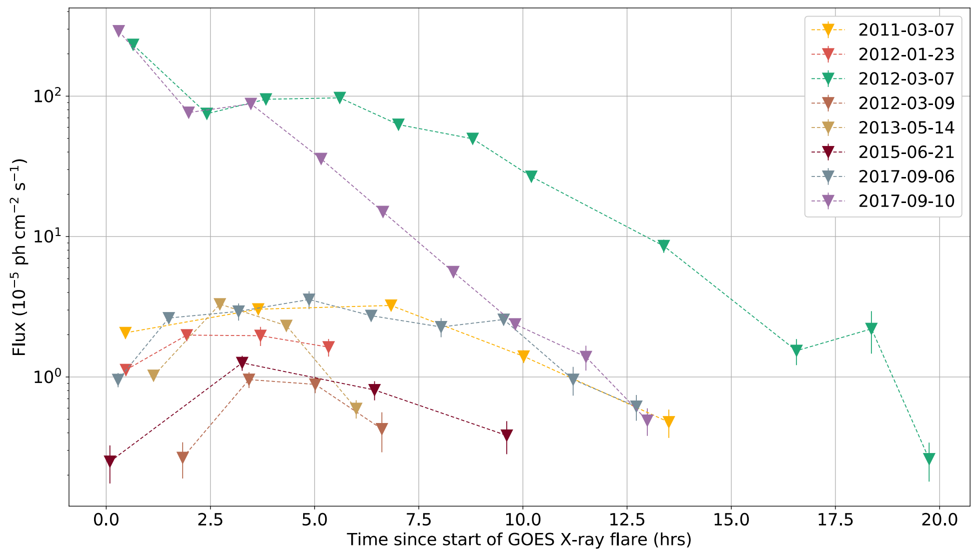

Figure 14. The time profiles of flux between 0.1 and 10 GeV for each FLSF lasting two or more hours vs. the time since the start of the GOES X-ray flare. The typic rise and fall behavior of the γ-ray emission during the delayed phase is most evident for the cases where no prompt emission was present during the detection.

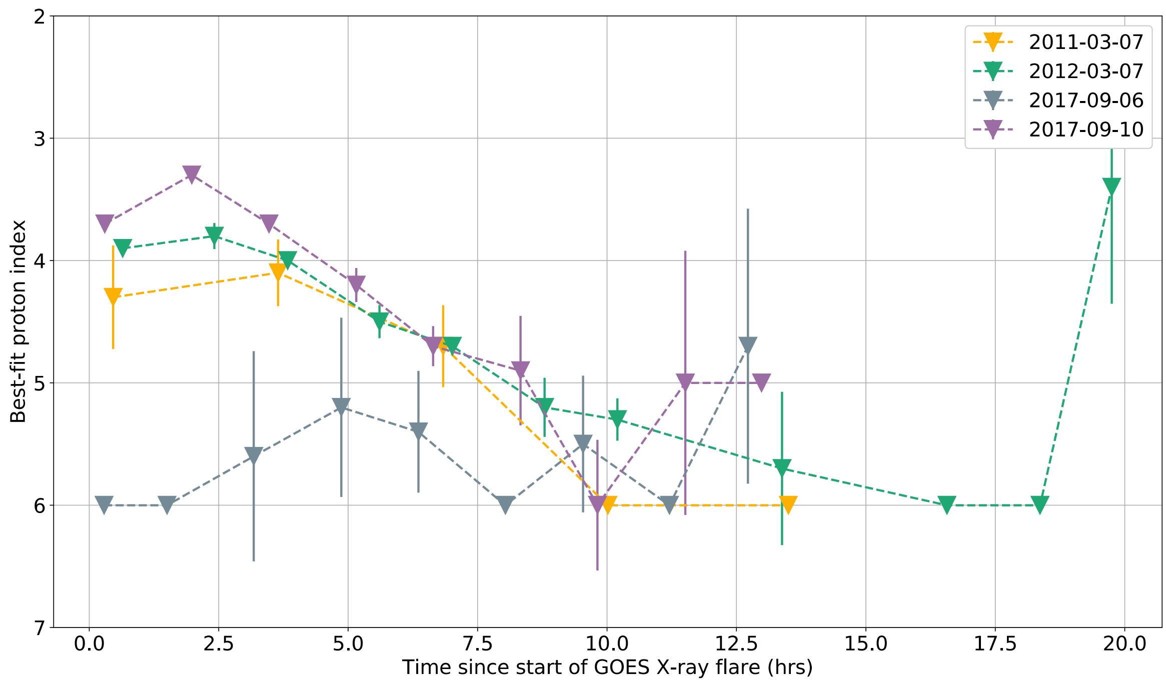

Figure 15. Variation with time (since the start of the GOES X-ray flare) of the best-fit proton spectral index for the four FLSFs for which a statistically meaningful measurement can be made.

The FLSF LLE catalog results are reported in Table 3. Three of the flares detected with LLE were outside the nominal LAT FoV. For the 11 flares in the FoV, five were not detected above 60 MeV by the SunMonitor analysis, and an upper limit was obtained for the time window when the flare happened. For the six flares detected with both analyses in the same time window, the >100 MeV fluxes reported in the SunMonitor results (Table 1) are the average over the time window, and the >100 MeV fluxes obtained through the LLE approach are listed in Table 3.

The durations for the flares detected with the SunMonitor range from 0.6 to 20.3 hr, whereas the LLE detected flares have durations ranging from 10 to 400 s (see Figure 12). Both the >100 MeV peak γ-ray fluxes and the total number of >500 MeV protons needed to produce the observed γ-ray emission for all of the FLSFs in the catalog span over four orders of magnitude (see Figure 13).

Eight of the 45 FLSFs have durations of two hours or more. Their >100 MeV fluxes as a function of time (since the start of the associated GOES X-ray flare) are shown in Figure 14. The time profiles of all these delayed FLSFs follow a rise-and-fall behavior. However, the rise times to reach the peak flux and the fall times vary significantly from flare to flare. For example, the FLSF 2017 September 10 has a rise time of ≈1.5 hr while the FLSF 2017 September 6 takes ≈4.5 hr to reach its peak. The peak flux values also vary from flare to flare by up to two orders of magnitude, emphasizing the wide variety of these

Table 4
Multiwavelength Associations for All of the FLSFs in This Work

Name	Total Duration (hr)	Flare Type	GOES Start (UT)	GOES Class	CME Speed ($km\ s^{-1}$)	CME First C2 app.(UT)
FLSF 2010 Jun 12	30[a]	LLE-Prompt[a]	2010 Jun 12 00:30	M2.0	486	2010 Jun 12 01:3
FLSF 2011 Mar 7	15.8 ± 3.1	Delayed	2011 Mar 7 19:43	M3.7[c]	2125	2011 Mar 7 20:0
FLSF 2011 Jun 7	6.0 ± 2.2	Delayed	2011 Jun 7 06:16	M2.5	1255	2011 Jun 7 06:4
FLSF 2011 Aug 4	2.3 ± 0.7	Delayed	2011 Aug 4 03:41	M9.3	1315	2011 Aug 4 04:1
FLSF 2011 Aug 9	0.87 ± 0.34	Prompt Short-Delayed[a]	2011 Aug 9 07:48	X6.9	1610	2011 Aug 9 08:1
FLSF 2011 Sep 6	2.0 ± 1.4	LLE-Prompt Short-Delayed[a]	2011 Sep 6 22:12	X2.1	575	2011 Sep 6 23:0
FLSF 2011 Sep 7	2.02 ± 0.35	Delayed	2011 Sep 7 22:32	X1.8	792	2011 Sep 7 23:0
FLSF 2011 Sep 24	1.2 ± 0.7	LLE-Prompt Short-Delayed[a]	2011 Sep 24 09:21	X1.9	1936	2011 Sep 24 09:
FLSF 2012 Jan 23	5.9 ± 1.0	Delayed	2012 Jan 23 03:38	M8.7	2175	2012 Jan 23 04:0
FLSF 2012 Jan 27	6.8 ± 1.5	Delayed	2012 Jan 27 17:37	X1.7	2508	2012 Jan 27 18:2
FLSF 2012 Mar 5	4.4 ± 1.2	Delayed	2012 Mar 5 02:30	X1.1	1531	2012 Mar 5 04:0
FLSF 2012 Mar 7	20.3 ± 0.8	Delayed	2012 Mar 7 00:02	X5.4[c]	2684[b]	2012 Mar 7 00:2
FLSF 2012 Mar 9	7.2 ± 1.7	No-Prompt Delayed	2012 Mar 9 03:22	M6.3	950	2012 Mar 9 04:2
FLSF 2012 Mar 10	6 ± 4	Delayed	2012 Mar 10 17:15	M8.4	1296	2012 Mar 10 18:0
FLSF 2012 May 17	2.6 ± 0.5	Delayed	2012 May 17 01:25	M5.1	1582	2012 May 17 01:
FLSF 2012 Jun 3	1.9 ± 1.5	LLE-Prompt Short-Delayed[a]	2012 Jun 3 17:48	M3.3	605	2012 Jun 3 18:1
FLSF 2012 Jul 6	1.27 ± 0.35	Delayed	2012 Jul 6 23:01	X1.1	1828	2012 Jul 6 23:24
FLSF 2012 Aug 6	30[a]	LLE-Prompt[a]	2012 Aug 6 04:33	M1.6	198	2012 Aug 6 05:1
FLSF 2012 Oct 23	1.9 ± 0.5	LLE-Prompt Delayed[a]	2012 Oct 23 03:13	X1.8	L	
FLSF 2012 Nov 13	0.041 ± 0.006	Prompt	2012 Nov 13 01:58	M6.0	851	2012 Nov 13 02:2
FLSF 2012 Nov 27	0.166 ± 0.025	Prompt Short-Delayed	2012 Nov 27 15:52	M1.6	L	
FLSF 2013 Apr 11	0.38 ± 0.27	No-Prompt Short-Delayed	2013 Apr 11 06:55	M6.5	861	2013 Apr 11 07:2
FLSF 2013 May 13a	4.0 ± 1.3	Delayed	2013 May 13 01:53	X1.7	1270	2013 May 13 02:0
FLSF 2013 May 13b	6.1 ± 2.2	Delayed	2013 May 13 15:48	X2.8	1850	2013 May 13 16:0
FLSF 2013 May 14	5.9 ± 0.5	No-Prompt Delayed	2013 May 14 00:00	X3.2	2625	2013 May 14 01:2
FLSF 2013 May 15	3.5 ± 0.5	No-Prompt Delayed	2013 May 15 01:25	X1.2	1366	2013 May 15 01:4
FLSF 2013 Oct 11	0.38 ± 0.32	BTL Short-Delayed	2013 Oct 11 07:01	M4.9*	1200	2013 Oct 11 07:2
FLSF 2013 Oct 25a	1.4 ± 0.5	Delayed	2013 Oct 25 07:53	X1.7	587	2013 Oct 25 08:1
FLSF 2013 Oct 25b	10[a]	LLE-Prompt[a]	2013 Oct 25 20:54	M1.9	L	
FLSF 2013 Oct 28a	70[a]	LLE-Prompt[a]	2013 Oct 28 01:41	X1.0	695	2013 Oct 28 02:2
FLSF 2013 Oct 28b	50[a]	LLE-Prompt[a]	2013 Oct 28 04:32	M5.1	1201	2013 Oct 28 04:4
FLSF 2013 Oct 28 c	1.6 ± 0.6	Delayed	2013 Oct 28 14:46	M2.7[c]	812	2013 Oct 28 15:3
FLSF 2013 Oct 28d	50[a]	LLE-Prompt[a]	2013 Oct 28 20:48	M1.5	771	2013 Oct 28 21:2
FLSF 2014 Jan 06	0.27 ± 0.04	BTL Short-Delayed	2014 Jan 06 07:40	X3.5*	1402	2014 Jan 06 08:0
FLSF 2014 Jan 07	1.05 ± 0.26	Delayed	2014 Jan 07 18:04	X1.2	1830	2014 Jan 07 18:2
FLSF 2014 Feb 25	8.4 ± 1.8	LLE-Prompt Delayed[a]	2014 Feb 25 00:39	X4.9	2147	2014 Feb 25 01:2
FLSF 2014 Jun 10	1.9 ± 0.6	LLE-Prompt Delayed[a]	2014 Jun 10 12:36	X1.5	1469	2014 Jun 10 13:3
FLSF 2014 Jun 11	0.23 ± 0.17	Short-Delayed	2014 Jun 11 08:59	X1.0	829	2014 Jun 11 09:2
FLSF 2014 Sep 1	2.5 ± 1.2	BTL Delayed	2014 Sep 1 10:58	X2.4*	1901	2014 Sep 1 11:1
FLSF 2014 Sep 10	0.30 ± 0.06	Short-Delayed	2014 Sep 10 17:21	X1.6	1071[b]	2014 Sep 10 17:2
FLSF 2015 Jun 21	11.5 ± 2.5	Prompt Delayed	2015 Jun 21 02:04	M2.7[c]	1366	2015 Jun 21 02:3
FLSF 2015 Jun 25	2.4 ± 1.3	Delayed	2015 Jun 25 08:02	M7.9	1627	2015 Jun 25 08:3

Table 4
(Continued)

Name	Total Duration (hr)	Flare Type	GOES Start (UT)	GOES Class	CME Speed (km s^{-1})	CME First C2 app.(UT)
FLSF 2017 Sep 6a	0.169 ± 0.025	Prompt	2017 Sep 6 08:57	X2.2	391	2017 Sep 6 09:4
FLSF 2017 Sep 6b	13.33 ± 0.32	Delayed	2017 Sep 6 11:53	X9.3[c]	1571	2017 Sep 6 12:2
FLSF 2017 Sep 10	13.9 ± 1.2	Prompt Delayed[a]	2017 Sep 10 15:35	X8.2	3163	2017 Sep 10 16:0

Note. Entries with an * indicate that the duration is in seconds and not in hours because these are LLE-only flare detections; [a] indicates that there is also an LLE detection
standard analysis; [b] indicates cases with two CMEs and the CME width is marked H for halo CMEs, which corresponds to a width of 360°; [c] indicates cases where multiple C
an increase in the SEP energy channel was present.

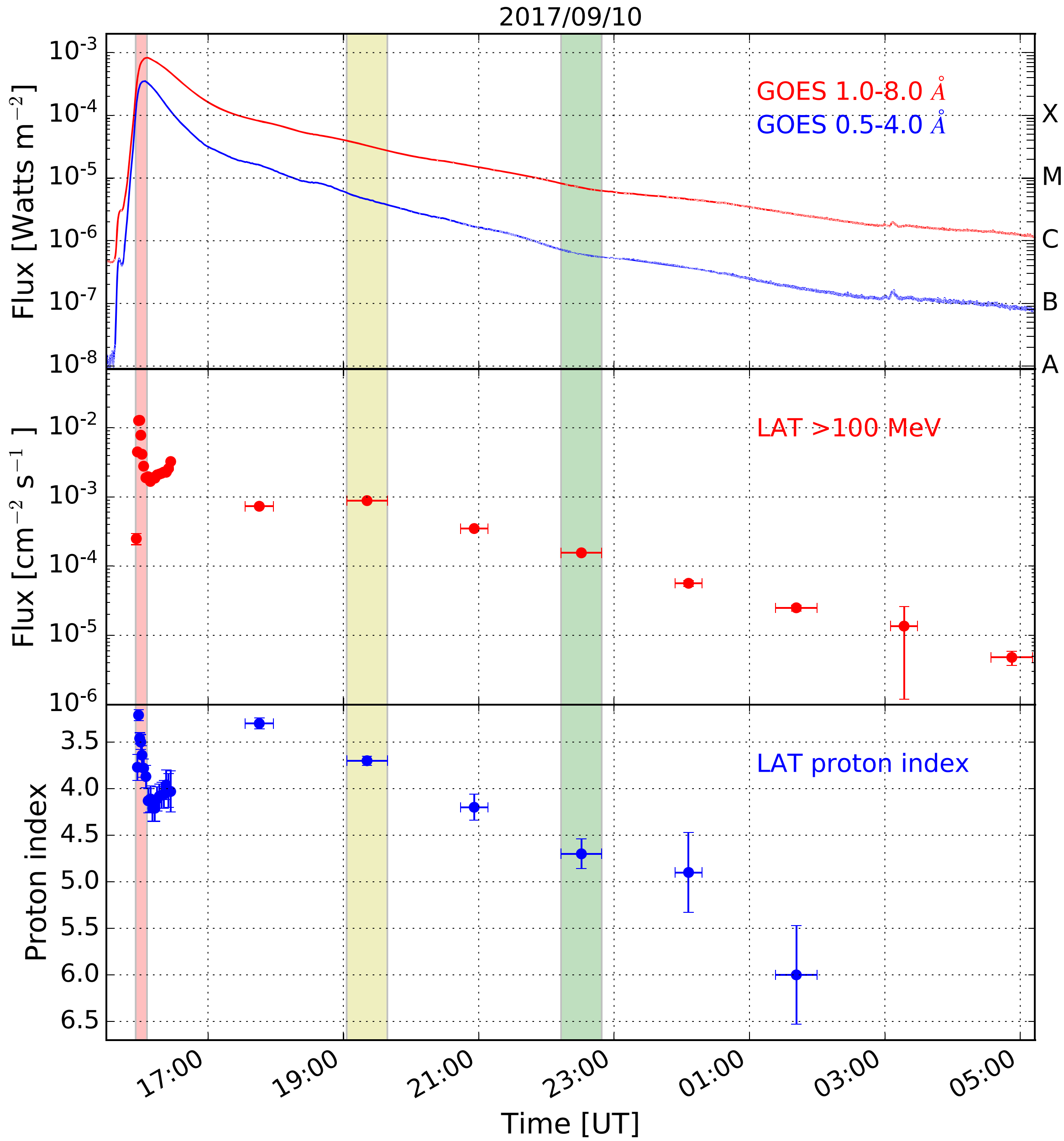

Figure 16. Composite lightcurve for the FLSF 2017 September 10 with data from GOES X-rays, Fermi-LAT >100 MeV flux, and the best proton index inferred from the LAT γ-ray data. The figure is taken from Omodei et al. (2018). The evolution of the proton index shows three distinct phases: softening during the prompt-impulsive phase, a plateau, and another softening during the decay phase. The three color bands represent the time windows over which we performed the localiz of the emission.

delayed flares. The two brightest flares in Figure 14 were coincident with very strong SEP events; Ground Level Enhancement (GLE) #72 in the case of the FLSF 2017 September 10 and a sub-GLE event in the case of the FLSF 2012 March 7.[69] Coincidentally, the γ-ray fluxes for these two flares are more than an order of magnitude higher than the other events. In Table 4, we list some multiwavelength associations with the FLSFs presented in this work. In particular, we include GOES X-ray flares, CMEs, SEPs, and HXR counterparts to the gamma-ray flares.

For the FLSFs with more than four SunMonitor detection windows, it is possible to study the variation of the proton index with time. In Figure 15, we show the accelerated proton spectral index as a function of time since the start of the GOES X-ray flare (assuming that the γ-ray emission is due to pion decay). The statistical uncertainties limit the amount of information available from the time variation of the proton indices. However, the data suggest that the proton spectra tend to gradually steepen (get softer), following a trend similar to the γ-ray fluxes for these delayed flares.

For the extremely bright FLSF 2017 September 10, both the prompt and delayed phases were well observed by the LAT, and we are not limited by statistics. The data from this flare show three phases in the evolution of the proton index over the almost two hours of γ-ray emission (see Figure 16). This flare

[69] GLEs are sudden increases in the cosmic-ray intensity recorded by ground-based detectors. The number following the GLE indicates the number of GLEs that have been observed since 1956; see the GLE database http://gle.oulu.fi for more details.

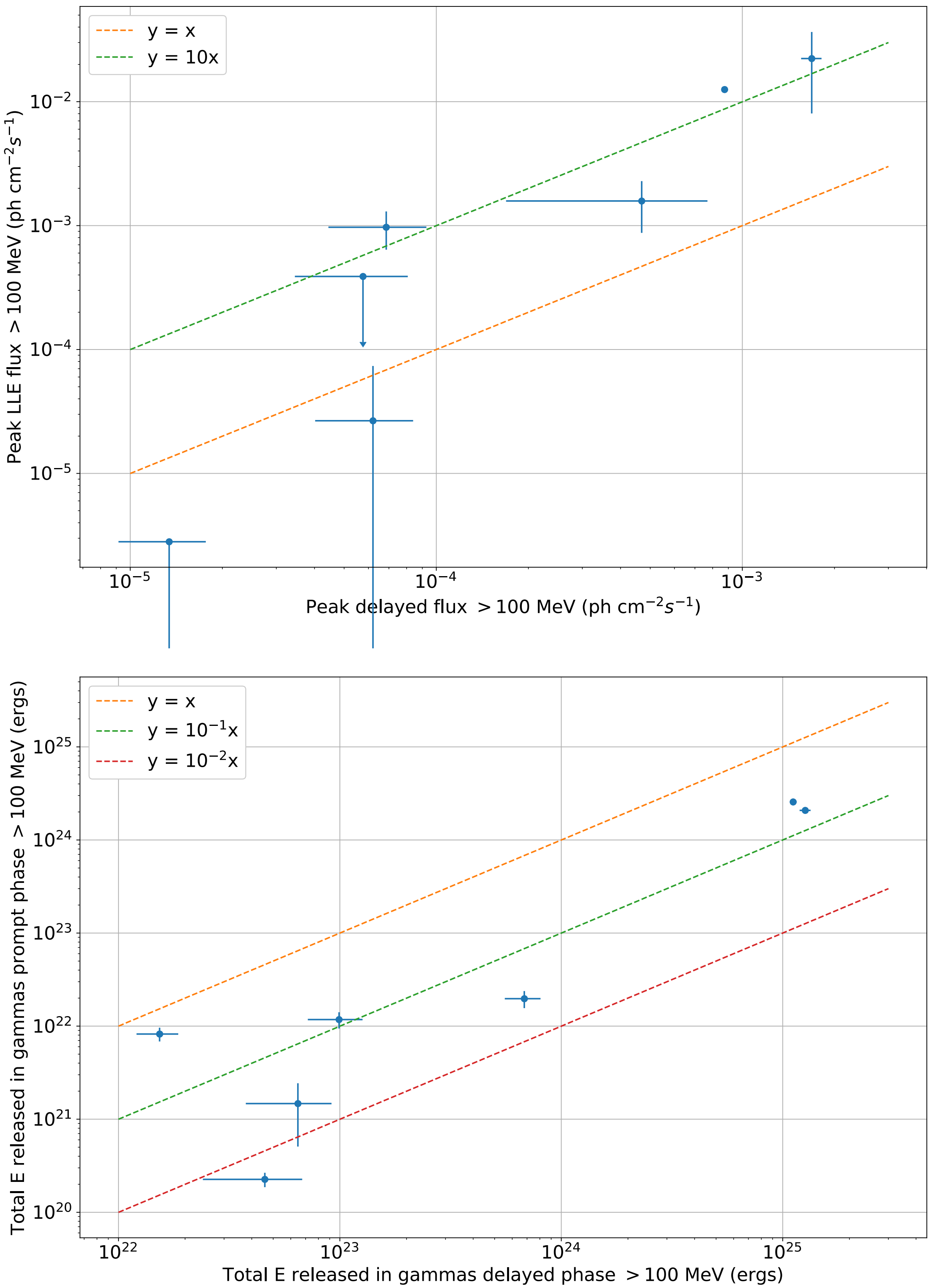

Figure 17. Scatter plot of the peak flux during the prompt phase vs. the peak flux during the delayed phase for the seven FLSFs with both the prompt and delayed phases observed fully. The prompt peak fluxes tend to be higher than those during the delayed phase, in some cases up to more than 10 times. Bottom panel: sca plot of the total energy released in γ-rays above 100 MeV during the prompt and delayed phases. The total energy released during the delayed phase is on averag about 10 times larger than the prompt phase.

was also associated with GLE #72, and Kocharov et al. (2020) show that these phases correspond to separate components of the GLE.

Solar cycle 24 has been particularly poor in GLE events. Only two have been firmly identified: GLE #71 and #72, which occurred on 2012 May 17 and 2017 September 10. Both

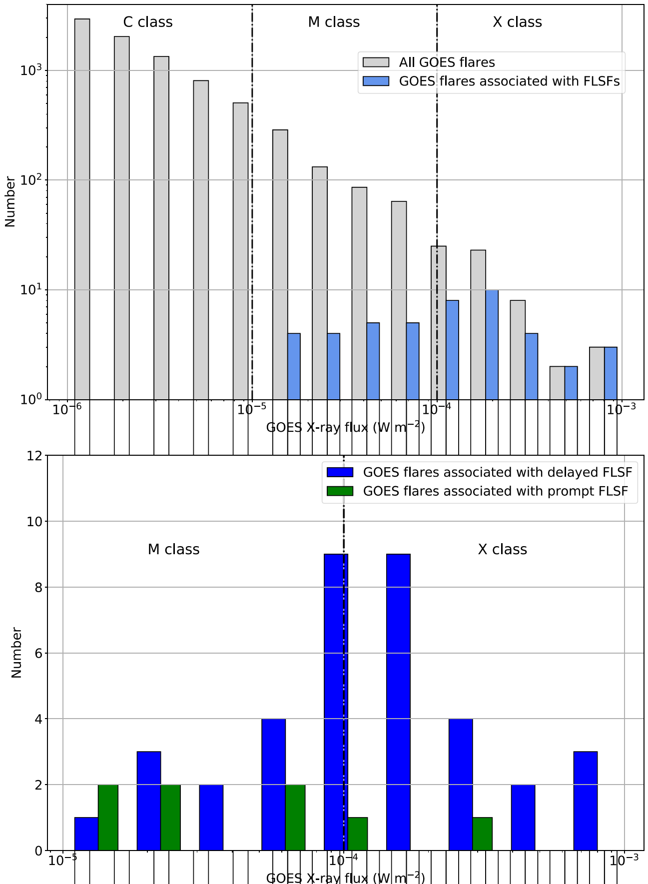

Figure 18. Top panel: distribution of the GOES class for all of the X-ray flares of solar cycle 24 (in gray) and for the FLSFs (light blue). Bottom panel: distribution of the GOES class for the FLSFs separated by type delayed (blue) and prompt flares (green).

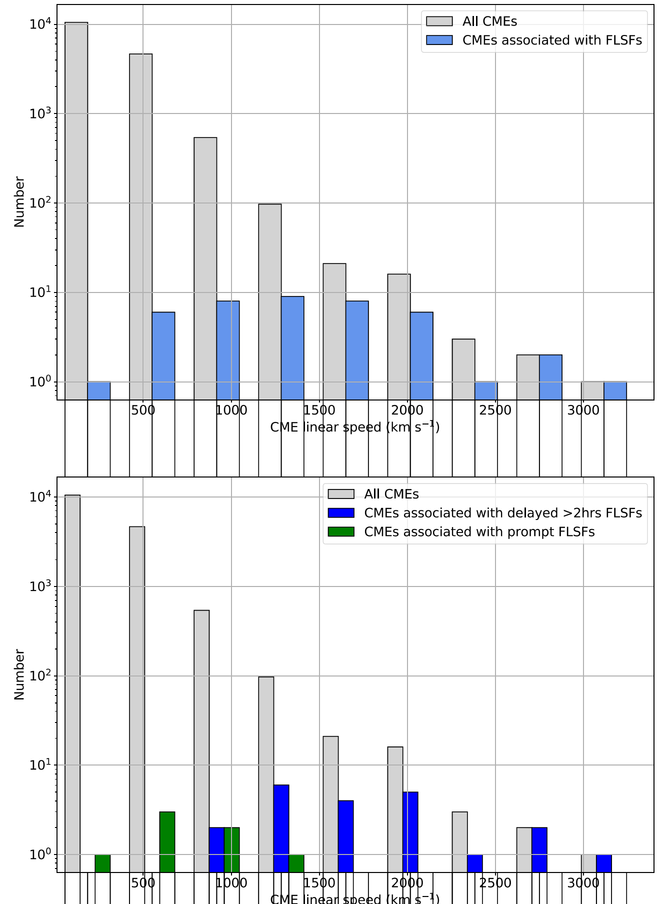

Figure 19. Top panel: distribution of the CME linear speed for all of solar cycle 24 (in gray) and for all the FLSFs in this work (light blue). Bottom panel: distribution of the CME linear speed for FLSFs classified as delayed (blue) and FLSFs classified as prompt (green). The mean speed for the delayed flares is 1535 km s^{-1} and for the prompt flares is 656 km s^{-1}. As in the top panel, the gray histogram represents the CME linear speed for all of the CMEs of solar cycle 24 (whose mean speed is 342 km s^{-1}).

events were detected with the Fermi-LAT. In addition to GLEs, five “sub-GLE” events have been identified. Sub-GLE events are those detected only by high-elevation neutron monitors and correspond to less energetic events, extending to a few hundred MeV (Poluianov et al. 2017). They occurred on 2012 January 27, 2012 March 7, 2014 January 06, 2015 June 07, and 2015 October 29 at levels of relative increase in neutron flux of 5%, 5%, 4%, 8%, and 7%, respectively (smaller than the relative increase of 17% for GLE#71). The first three correspond to flares in the FLSF catalog, but no emission was detected for the last two.

Flares with both the LLE-prompt and delayed phases detected by the LAT allow a comparison of the prompt and delayed emission characteristics within the same flare. Seven flares in the catalog (2011 September 6, 2011 September 24, 2012 June 3, 2012 October 23, 2014 February 25, 2014 June 10, and 2017 September 10) satisfy this criterion. For these flares, we found the peak flux value for the prompt phase by fitting the LLE data at the peak of the lightcurve with two models: a simple power law or a power law with an exponential cutoff using the xspec analysis package.[70] The correlation between the peak fluxes of the prompt and delayed phases is shown in the top panel of Figure 17 illustrating that, on average, the prompt peak flux is up to 10 times higher than the peak of the delayed emission. The bottom panel of this figure shows the correlation between the total γ-ray energies (>100 MeV), showing a larger dispersion and a total energy released during the delayed phase that, on average, is about 10 times larger than that in the prompt phase.

The FLSFs in the catalog are almost evenly distributed between GOES M- and X-class flares (in the 0.5–10 keV energy range), with 25 flares associated with the X class and 20 associated with the M class (see top panel of Figure 18 where the gray distribution represents all of the M- and X-class GOES flares that occurred during the time period considered in this paper). As can be seen in the bottom panel of Figure 18, the FLSFs of delayed type are evenly distributed between the M- and X-class flares while the prompt-type flares are mostly associated with M GOES-class flares (75% of the flares are M class). These distributions also illustrate how the increase in sensitivity of the LAT with respect to the previous γ-ray detectors has allowed >100 MeV emission to be detected over a wider range of GOES X-ray flares. Furthermore, when combining the information from Figures 18 and 19, it appears that the presence of a fast CME is more relevant for the delayed-type flares than the brightness of the associated X-ray flare.

During Cycle 24, the number of GOES M-class and X-class flares in the period covered by this catalog (2010 January–2018

[70] xspec model pegpwrlw and pegpwrlw*highecut

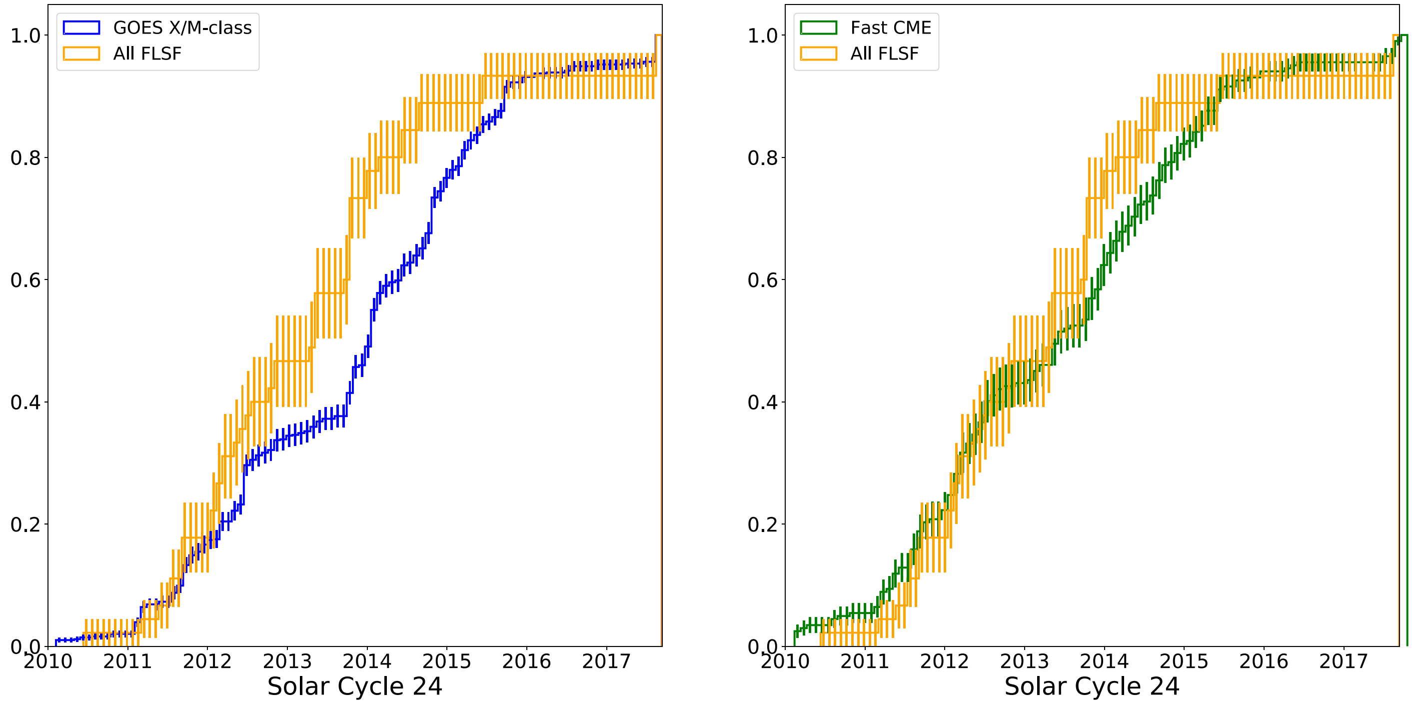

Figure 20. Cumulative number of FLSFs as a function of time compared with the distribution for M-/X-class GOES flares (left) and fast CME (linear speed >1000 km s^{-1}) events (right).

January) was approximately the same in the first half as in the second (384 and 389, respectively), while the majority of fast CME events (those with speed >1200 km s^{-1}) happened in the earlier half (2010 January–2014 January; 61 versus 35). A similar behavior was observed for major SEP events (30 in the first half and 12 in the second half of the cycle). Interestingly, the number of FLSFs is also larger in the first half of the cycle, with 33 flares, while only 12 occurred in the second half. To quantify this behavior, we show in Figure 20 the cumulative distributions of XRT flares and fast CME (linear speed >1000 km s^{-1}) events compared with the distribution of FLSFs. The latter seems to be in much better agreement with the distribution of fast CME events, with a Kolmogorov–Smirnov test p value of 0.15, while the comparison of XRT flares with FLSFs gives a p value of 4.6×10^{-4}. This result is also suggesting that high-energy solar flares have a stronger association with fast CMEs rather than with bright X-ray flares.

4.1. FLSF Active Region Positions

The positions on the solar surface of the ARs associated with the FLSFs are plotted together with the M-/X-class flares detected by Hinodes's XRT (Sakurai 2008) in Figure 21. Three BTL flares, whose position was inferred from STEREO, appear with longitudes smaller or greater than −90° and +90°. The distribution in longitude is rather uniform, with the same number of flares in positive and negative longitudes between −90° and +90°. However, there is an asymmetry in the distributions in latitude, with a preponderance of FLSFs (~65%) in the northern hemisphere, while the opposite is true for the XRT flares. This asymmetry is also evident in Figure 22, where we plot the positions of FLSF ARs as a function of time, illustrating the so-called butterfly pattern, with ARs migrating toward the equator as the solar cycle evolves.

4.2. Flare Series

A notable feature of the FLSF population is that more than half (25 out of 45) are part of a cluster of flares originating from the same AR (see Table 5). It is common for an AR to be the source of several flares, but the high fraction of such clusters in the FLSF catalog might indicate that some ARs have the right conditions to be associated with the production of γ-rays. The most notable series happened from 2012 March 5 to 2012 March 10 and 2013 March 13 to 2013 March 15, each with four FLSFs. All of these flares were associated with fast CMEs, and both series produced strong and long-lasting SEP events. They all yielded delayed FLSF γ-ray emission lasting more than three hours. In addition, three of the eight flares were identified as having no >100 MeV γ-rays detected during the prompt phase; only delayed emission was detected. Only one additional flare behaved this way, FLSF 2013 April 11, which was found to have a short delayed emission and no prompt emission. This could indicate that the presence of previous SEP events and multiple fast CMEs is more important for the production of long-lasting γ-ray emission than the presence of impulsive HXRs produced by high-energy electrons.

4.3. Gamma-Ray Localization

The Fermi-LAT is the first telescope capable of determining the centroid of >100 MeV emission from solar flares. The position of the emission centroid on the solar disk can yield valuable information on where on the photosphere the precipitating ions produce the high-energy γ-rays.

For the majority of the FLSFs in the catalog, the 68% error on the emission centroid is larger than 500″, and therefore, it becomes difficult to distinguish a specific region on the solar disk from which the emission is originating. For eight of the FLSFs, the 68% error radius is ≲365″ (roughly a third of the solar disk), providing meaningful constraints on the location of

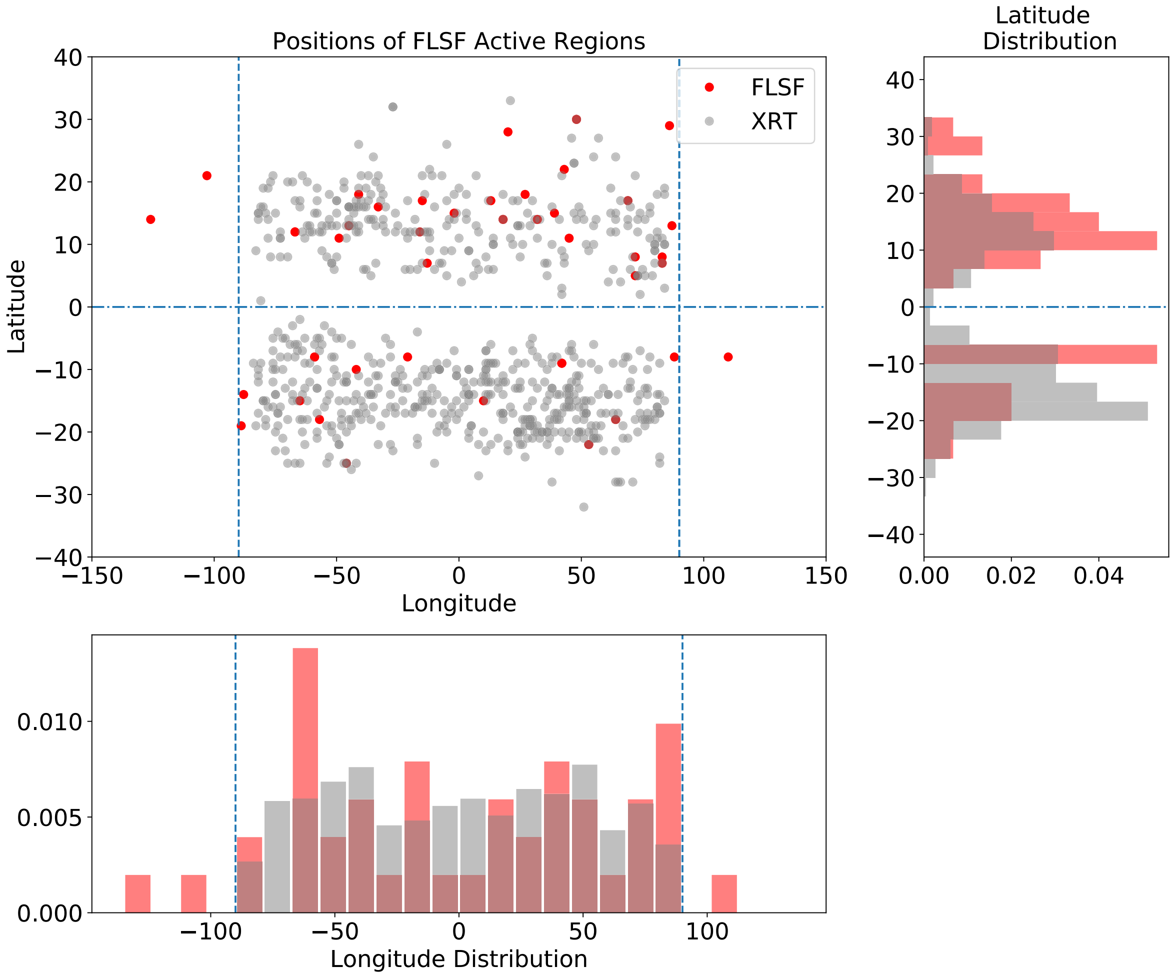

Figure 21. Positions of active regions associated with FLSFs (red) and M-/X-class XRT flares (gray). Longitudes beyond −90° and +90° correspond to BTL flares. The right-hand panel shows the latitude distribution of the AR positions, illustrating the asymmetry in the population. 64% of the ARs from which the FLSFs originat are located in the northern heliosphere whereas 62% of the ARs from which the XRT flares originate are located in the southern heliosphere.

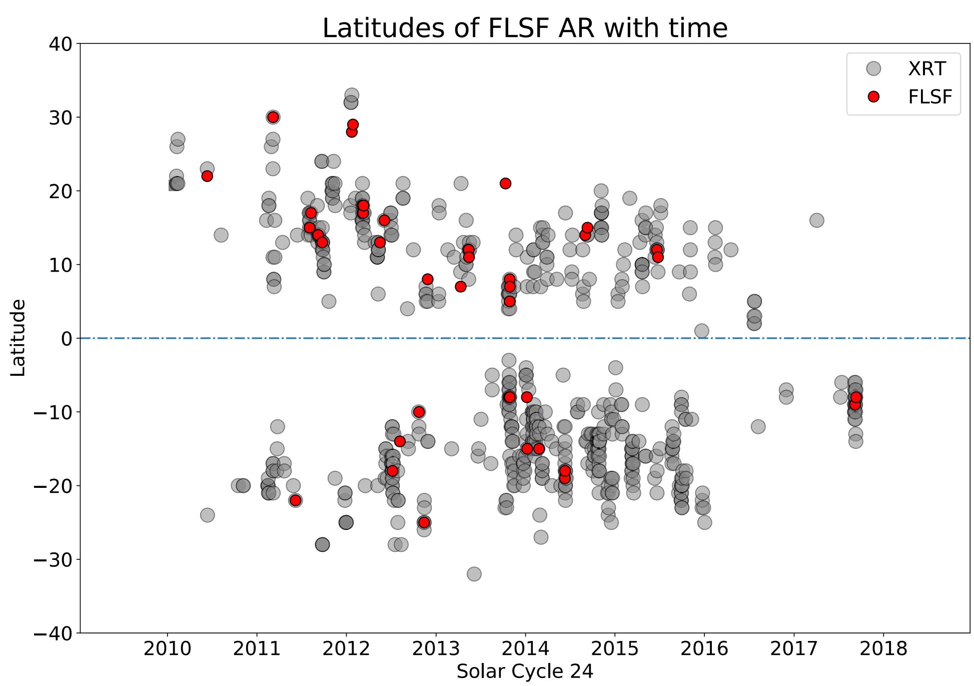

Figure 22. Positions of ARs associated with FLSF (red) and M-/X-class GOES flare (gray) as a function of time. The distribution of positions follows the so-called butterfly pattern, i.e., at the beginning of a new solar cycle, sunspots tend to form at high latitudes, but as the cycle reaches its maximum the sunspots tend to form lower latitudes.

Table 5
List of FLSFs from Similar Active Regions

Name	Flare Type	Duration (hr)	CME Speed (km s^{-1})	Width	GOES Class	SEP Emax (MeV)	HXR Emax (keV)	AR	AR pos
FLSF 2011 Sep 6	Prompt Delayed	0.6	575	H	X2.1	100	1000	11283	N14W18
FLSF 2011 Sep 7	Delayed	1.9	792	290	X1.8	50‡	500	11283	N14W32
FLSF 2012 Jan 23	Delayed	5.8	2175	H	M8.7	100	>100	11402	N28W20
FLSF 2012 Jan 27	Delayed	7.3	2508	H	X1.7	605	>100	11402	N29W86
FLSF 2012 Mar 5	Delayed	5.4	1531	H	X1.1	40‡	>100	11429	N18E41
FLSF 2012 Mar 7	Delayed	20.2	2684*	H	X5.4*	605	1000	11429	N17E15
FLSF 2012 Mar 9	Delayed only	7.3	950	H	M6.3	100‡	>100	11429	N17W13
FLSF 2012 Mar 10	Delayed	6.0	1296	H	M8.4	100‡	>50	11429	N18W27
FLSF 2013 May 13	Delayed	3.4	1270	H	X1.7	60	>300	11748	N12E67
FLSF 2013 May 13	Delayed	5.4	1850	H	X2.8	60	800	11748	N12E67
FLSF 2013 May 14	Delayed only	6.7	2625	H	X3.2	60	500	11748	N12E67
FLSF 2013 May 15	Delayed only	3.6	1366	H	X1.2	50	100	11748	N11E49
FLSF 2013 Oct 25	Delayed	1.1	587	H	X1.7	60	300	11882	S08E59
FLSF 2013 Oct 25	Prompt	0.1	L		M1.9	60‡	100	11882	S08E59
FLSF 2013 Oct 28	Delayed	1.3	812	H	M2.7*	60	50	11882	S08E21
FLSF 2013 Oct 28	Prompt	0.3	695	H	X1.0	0	1000	11875	N05W72
FLSF 2013 Oct 28	Prompt	0.1	1201	315	M5.1	0	1000	11875	N08W72
FLSF 2013 Oct 28	Prompt	0.1	771	284	M1.5	100‡	100	11875	N07W83
FLSF 2014 Jun 10	Prompt Delayed	1.8	1469	H	X1.5	60	1000	12087	S19E89
FLSF 2014 Jun 11	Delayed	0.5	829	130	X1.0	0	1000	12087	S18E57
FLSF 2015 Jun 21	Prompt Delayed	10.2	1366	H	M2.7*	10	>50	12371	N12E16
FLSF 2015 Jun 25	Delayed	2.1	1627	H	M7.9	10	1000	12371	N11W45
FLSF 2017 Sep 6	Prompt	0.3	391	245	X2.2	0	300	12673	S09W42
FLSF 2017 Sep 6	Delayed	13.3	1571	H	X9.3*	100	>300	12673	S09W42
FLSF 2017 Sep 10	Prompt Delayed	13.6	3163	H	X8.2	605	3000	12673	S08W88

Note. * indicates several X-ray classes or CMEs during the duration of the γ-ray emission. ‡ indicates the previous presence of SEPs, without this event being an S event.

the emission centroid that can then be compared with the lower-energy flare emission sites. The localization results for these eight flares are given in Table 6. The first eight columns of Table 6 report the date and time window of the detection, position of the centroid of the >100 MeV emission in helioprojective coordinates (X, Y), the 68% and 95% uncertainty on the emission centroid, the AR number and position, and the angular distance and relative distance of the emission centroid from the AR.[71] The last column shows the ratio of this distance to the 95% error radius. We emphasize that the position and the confidence intervals in the table are derived by modeling the high-energy emission as a point source, i.e., with no geometric extent on the solar surface.

Three of the eight flares (FLSF 2012 March 7, FLSF 2014 February 25, and FLSF 2017 September 10) were sufficiently bright and long lasting to be localized in multiple SunMonitor time windows. The FLSF 2012 March 7 was an exceptional γ-ray flare in terms of both duration and brightness. The error radius was smaller than 300″ in four detection windows, and the emission centroid moved progressively across the solar disk over the ~10 hr of γ-ray emission, as shown in Figure 23. This flare was the first for which this behavior in >100 MeV γ rays could be observed, and it was interpreted as supporting evidence for the CME-driven shock scenario as the particle accelerator (Ajello et al. 2014). For FLSF 2014 February 25, the statistics were sufficient to provide meaningful localization in only two time intervals, and the emission centroid remained consistent with the AR position over three hours, as shown in Figure 24. Finally, FLSF 2017 September 10 was also an exceptionally bright flare, but, because the AR was located at the very edge of the western limb, it was impossible to observe any progressive motion of the γ-ray source. Throughout the 7 hr detection, the source centroid remained consistent with the AR position, as shown in Figure 25.

Two out of these eight flares originated from ARs whose position was located behind the visible solar disk, highlighting how bright these flares were regardless of the position of the AR. All eight FLSFs were classified as GOES X-class flares, with the exception of the BTL FLSF 2013 October 11 whose GOES classification of M4.9 is most likely an underestimation (Nitta et al. 2013; Pesce-Rollins et al. 2015). The peak γ-ray fluxes were all greater than 3 × 10^{-5} ph cm^{-2} s^{-1} and exposure times were all greater than 20 minutes, indicating that they are not impulsive flares. Five of the FLSFs originated from ARs from the eastern quadrant and three from the western quadrant of the solar disk.

4.4. GOES X-class Flares Not Detected by the LAT

In an attempt to characterize the solar flares associated with γ-ray detections, we can also examine the population of solar flares not detected by the Fermi-LAT above 30 MeV. During

[71] The position of the AR at the time of the GOES X-ray flare.

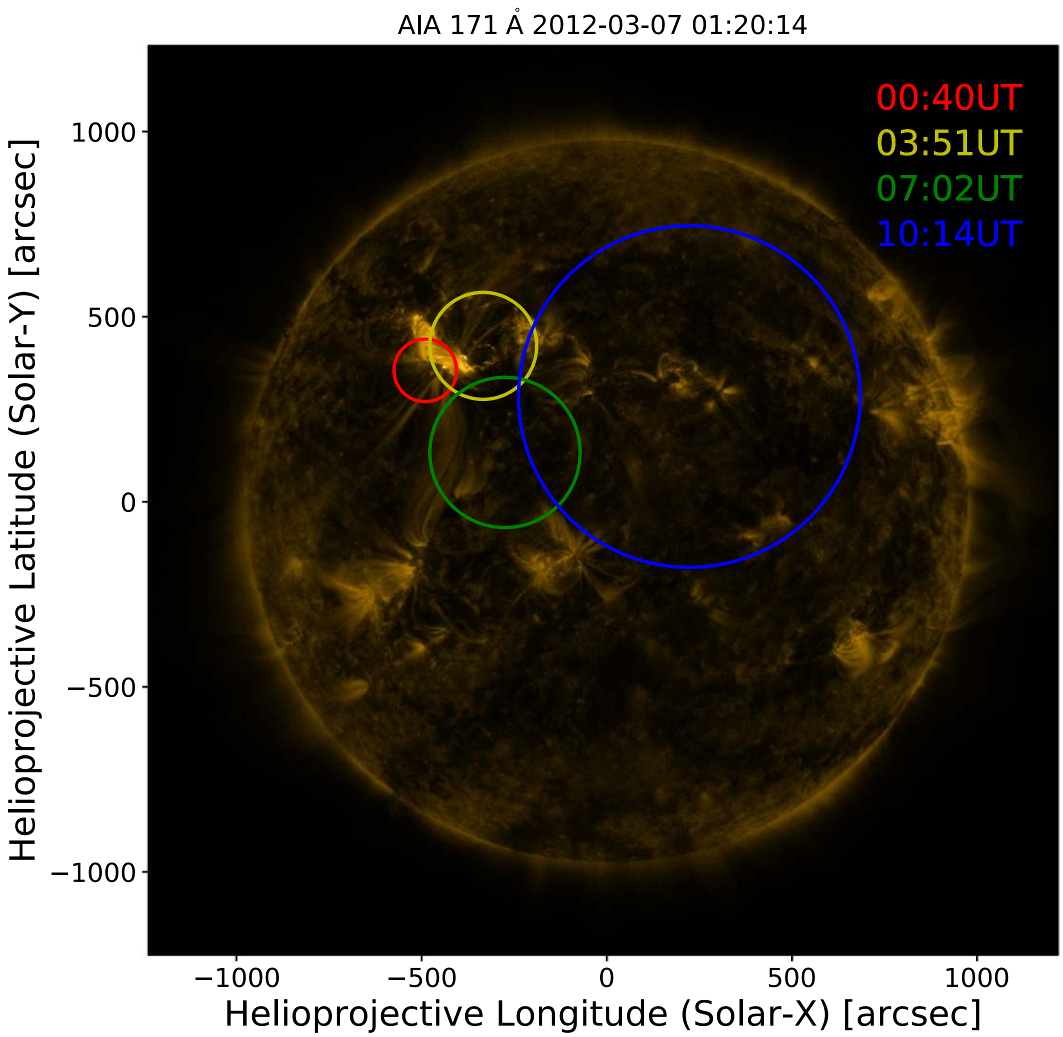

Figure 23. Fermi-LAT localization of the >100 MeV data in multiple time windows from the FLSF 2012 March 7. The error radii correspond to the 95% confidence region. The start of the time windows is annotated in the upper-right corner of the figure. The localization centroid is overplotted on the AIA 171 Å image of the Sun at the time of the flare.

the time period considered in this paper, there were a total of 772 M- and X-class flares (49 were X-class flares and 24 of these were associated with FLSFs).[72] In Table 7, we list only the 25 X-class flares not associated with a γ-ray detection and their possible associations with CMEs and SEP events. Figure 26 shows a scatter plot of CME speed versus GOES flux for all FLSFs and all the M-/X-class flares not detected by the LAT. We have labeled the four quadrants (I–IV) that indicate the population of flares classified as M/X class and whether they were associated with a CME with linear speed >/<1000 km s^{-1}. We report the fraction of LAT-detected flares over the total number of flares that fall within the quadrant. From this figure, it is possible to see that the most favorable condition for the LAT to detect γ-ray emission is for the flare to be of X class and be associated with a CME with linear speed greater than 1000 km s^{-1} (86% of the flares detected by the LAT) and that the least favorable condition (1% of the flares detected by the LAT) is diagonally opposite (i.e., M class and slow CME speed). The conditions in the off-diagonal quadrants appear to be equally favorable. Out of the three flares not detected by the LAT and in quadrant IV, the SunMonitor picked up a marginal detection in the three following observing windows (with a σ = 4.5, 4.0, 4.0) for the flare of 2011 September 22 that was associated with a halo CME with a linear speed of 1905 km s^{-1}.

[72] Here we include FLSF 2012 March 7; we associate the γ-ray emission with the X5.4 X-ray flare and with the CME with a linear speed of 2684 km s^{-1}. Two of the three BTL flares have an estimated GOES class of X3.5 and X2.4, but are not considered in this comparison because we do not have a catalog of X-class flares occurring BTL.

5. Summary and Discussion

Continuous monitoring of the Sun by Fermi-LAT has led to high-confidence detection of 45 solar flares with γ-ray emission above 60 MeV. With such a relatively sizable sample of flares, it is now possible to perform population studies of γ-ray solar flares. Based on the temporal characteristics and associations with multiwavelegth flaring activity, we have found that there are at least two distinct types of γ-ray emission in solar flares: prompt-impulsive and delayed-gradual. Within these two broad classes, we find a rich and diverse sample of events with a wide variety of characteristics. Of the 45 FLSFs discussed in this work, six have been detected only with a prompt-impulsive emission correlated with HXR emission (classified as prompt only), four have no γ-ray emission detected during the

Table 6
Localization Results for the FLSFs with 68% Error Radius <0°.1

Date and Time	Helio X (″)	Helio Y (″)	ERR 68 (″)	ERR 95 (″)	AR Number	AR Position	Angular Dist. (″)	Relative Dist. (95)
2011 Sep 6 22:11–22:47	219	533	139	220	11283	N14W18	382	1.7
2012 Mar 7 00:40–01:20	−562	231	56	84	11429	N17E15	45	0.5
2012 Mar 7 03:51–04:31	−300	342	84	144	11429	N17E15	143	1.0
2012 Mar 7 07:02–07:42	−320	20	126	203	11429	N17E15	331	1.6
2012 Mar 7 10:14–10:54	207	245	291	462	11429	N17E15	707	1.5
2012 Jul 6 23:20–00:08	530	−432	362	586	11515	S18W64	122	0.2
2013 May 14 02:43–03:31	−1137	333	314	504	11748	N12E67	279	0.6
2013 Oct 11 06:56–07:39	−930	311	151	263	BTL	N21E103	L	L
2014 Feb 25 01:09–01:29	−933	−347	92	147	11990	S15E65	63	0.4
2014 Feb 25 04:20–04:40	−982	−213	358	574	11990	S15E65	109	0.2
2014 Sep 1 11:02–11:18	−1126	−182	202	322	BTL	N14E126	L	L
2017 Sep 10 15:52–16:28	847	−207	59	95	12673	S08W88	72	0.8
2017 Sep 10 19:03–19:39	1034	−131	104	166	12673	S08W88	168	1.0
2017 Sep 10 22:13–22:49	1139	137	271	443	12673	S08W88	336	0.8

Note. We report the date and detection time window start and stop, LAT >100 MeV emission centroid position in Helio X and Y coordinates, the 68% and 95% error radius (in arcseconds), the AR number and position, the distance of the centroid from the active region, and the ratio of this distance to the 95% error radius.

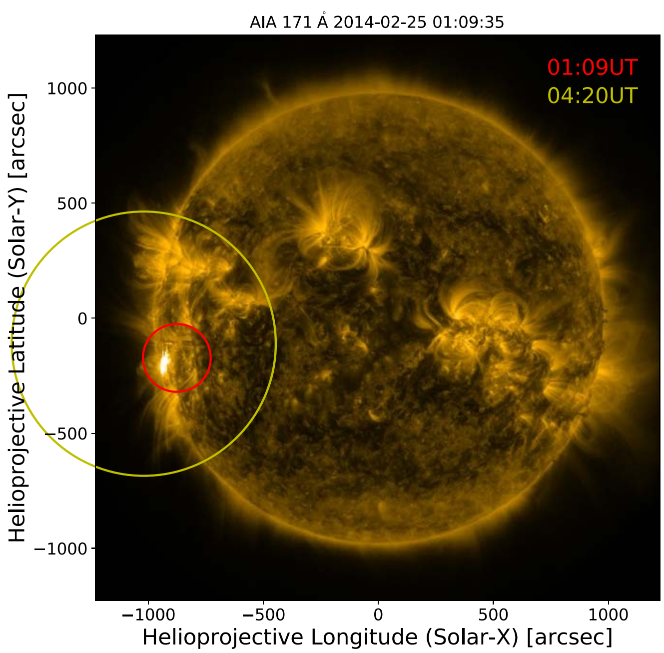

Figure 24. Fermi-LAT localization of the >100 MeV data in multiple time windows from the FLSF 2014 February 25. The error radii correspond to the 95% confidence region. The start of the time windows is annotated in the upper-right corner of the figure. The localization centroid is overplotted on the AIA 171 Å image of the Sun at the time of the flare.

impulsive HXR emission but were significantly bright after all other flare emission activities had ceased (classified as delayed only), and 10 have both prompt and delayed emission. For the remaining 25 flares with delayed emission, we cannot exclude the presence of prompt emission because the Sun was not in the FoV of the LAT during the impulsive HXR activity phase.

The most significant results presented in this work can be summarized as follows:

1. Emission above 60 MeV could be due to bremsstrahlung radiation produced by electrons of Lorentz factor $\gamma_e > 100$ with a relatively hard spectrum is most probably an unlikely scenario. This is because the acceleration of electrons to such energies is difficult due to high synchrotron losses. We find that emission due to the decay of pions (π^0, $\pi^{\pm}$) produced by > 300 MeV protons and ions, with a power-law spectrum of index ~4–5, extending up to 10s of GeV, produces a very good fit to all observed γ rays.
2. All of the FLSFs with LLE prompt emission (produced by >300 MeV ions) reach their peak within seconds of the 100–300 keV emission peak (produced by >100 keV electrons) observed with Fermi-GBM, implying that these ions and electrons are accelerated, transported, and interact with the ambient medium at the same time. Similar conclusions for the acceleration of lower-energy (1–30 MeV) ions were reached by Chupp (1987) and Hurford et al. (2006) based on the RHESSI imaging of the 2.223 MeV neutron-capture γ-ray line, and by Shih et al. (2009) who reported a tight correlation between the 2.223 MeV line fluence and the >300 keV electron bremsstrahlung fluence.
3. All but three of the flares in the FLSF catalog are associated with CMEs. The delayed-type flares are associated with faster CMEs (mean speed of 1535 km s^{-1}), whereas the prompt-type FLSFs are associated with slower CMEs (mean speed of 656 km s^{-1}).
4. One of the most important contributions of Fermi-LAT has been its ability to localize the centroids of high-energy γ-ray emission on the Sun. In most such cases, the initial centroid position is at or near the AR where the flare originated. In several long-lasting strong flares, there are clear indications of change of the centroid position with time, often away from the AR. This change is best observed in the strong, long-lasting FLSF 2012 March 7, where the centroid of >100 MeV emission gradually

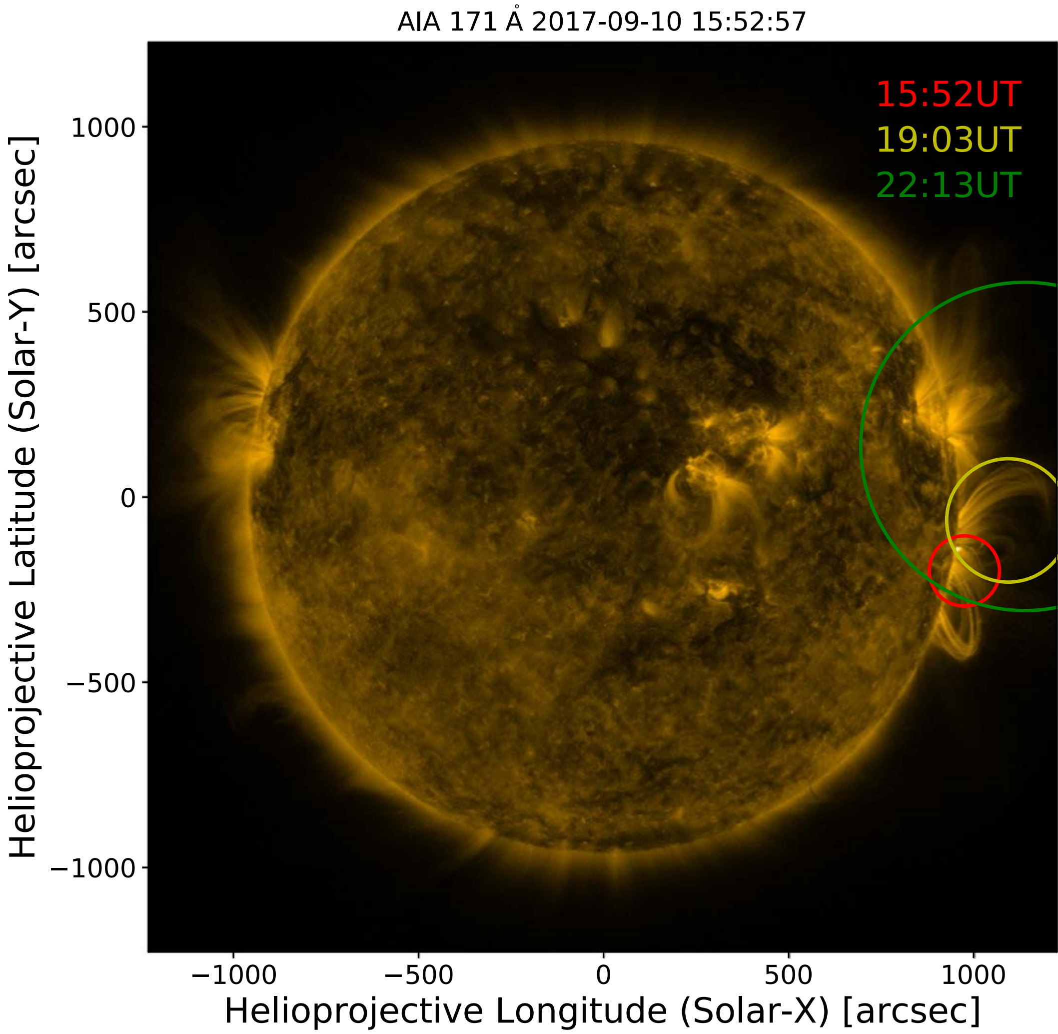

Figure 25. Fermi-LAT localization of the 100 MeV data in multiple time windows from the FLSF 2017 September 10. The error radii correspond to the 95% containment, the start of the time windows is annotated in the upper left-hand corner of the figure. The localization centroid is overplotted on the AIA 171 Å image of the Sun at the time of the flare.

migrates away from the AR up to tens of degrees. This indicates that the acceleration site of the γ-ray-producing high-energy ions is magnetically connected to regions on the photosphere far away from the initial AR.

5. Further evidence for this scenario comes from, for the first time, Fermi observation of GeV emission from three BTL flares including two-hour emission from FLSF 2014 September 1 originating 40° BTL. Localization of the γ-ray emission from two of these flares indicates that the emission occurred on the visible disk, again necessitating a way for the ions from the acceleration site to access regions on the visible disk (more than 40° away from the AR) to interact and to produce the observed γ-rays. Similar conclusions were also reached by Cliver et al. (1993) and Vestrand & Forrest (1993) for the observations with CGRO-EGRET of BTL flares with emission up to 100 MeV.
6. There is an asymmetry in the latitude distribution of the ARs from which the FLSFs originate, with 65% of the flares coming from the northern heliosphere. The opposite is true for the M-/X-class XRT flares detected during the same time interval. Shrivastava & Singh (2005) found that CMEs associated with Forbush decreases also come predominately from the northern heliosphere.
7. More than half of the FLSFs in this catalog are part of a series of flare clusters. The most notable clusters happened from 2012 March 5 to 2012 March 10 and from 2013 May 13 to 2013 May 15, with each consisting of four FLSFs. All of these flares were associated with fast CMEs, and both series produced strong and long-lasting SEP events. They all yielded delayed FLSF γ-ray emission lasting more than three hours. In addition, three of these eight flares showed no impulsive-phase γ-ray emission (only one other nonseries FLSF was found with similar properties). This could suggest that the presence of previous SEP events and multiple fast CMEs is more important for the production of long-lasting γ-ray emission than the presence of impulsive HXRs produced by high-energy electrons.
8. Seven FLSFs in the catalog are detected with both LLE-prompt and delayed phases, with the average peak flux of the prompt phase 10 times higher than that of the delayed phase. However, the total energy released during the delayed phase is 10–100 times larger than that during the prompt phase.

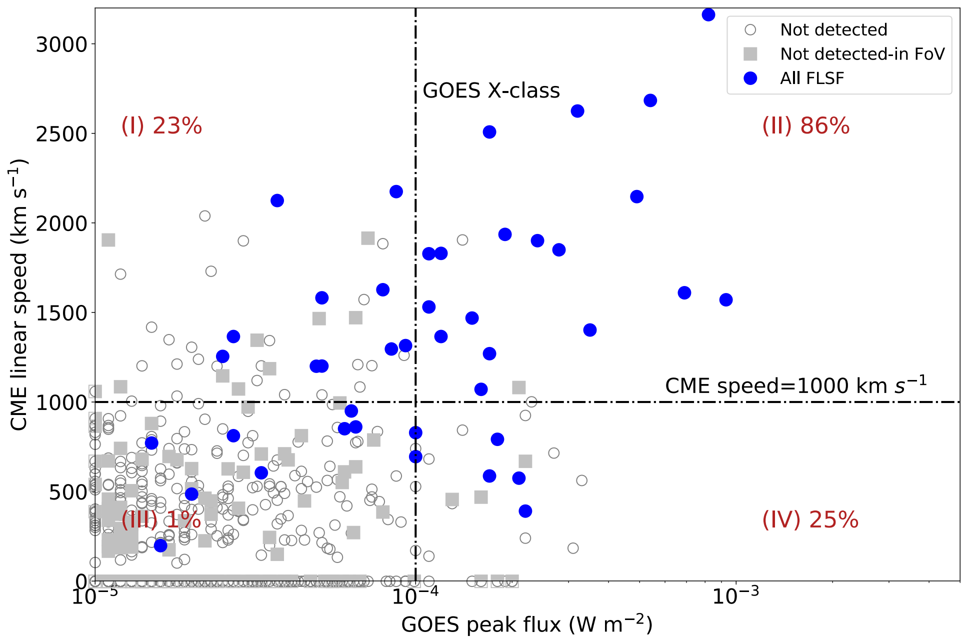

Figure 26. CME linear speed vs. GOES peak flux for all the FLSFs (blue points), M-/X-class flares not detected by the Fermi-LAT outside the LAT FoV (gray empty circles) and in the FoV (gray filled square) at the time of the GOES X-ray flare. The vertical dashed line indicates the border between M- and X-class GOES flares. The horizontal dashed line indicates a 1000 km s^{-1} CME speed. In each of the four quadrants (labeled I–IV), we indicate the fraction of flares detected by the LAT in that quadrant.

Table 7
X-class GOES Flares Not Associated with Any γ-Ray Emission above 30 MeV

GOES Start–Stop	GOES Class	CME First Appear. (UT)	CME Speed (km s^{-1})	CME Width (deg)	LAT Observable	SEP Event
2011 Feb 15 01:44–02:06	X2.2	2011 Feb 15 02:24	669	Halo	X	L
2011 Mar 9 23:13–23:29	X1.5	L	L	L	X	L
2011 Sep 22 10:29–11:44	X1.4	2011 Sep 22 10:48	1905	Halo	L	SEP
2011 Nov 3 20:16–20:32	X1.9	L	L	L	L	–
2012 Jul 12 15:37–17:30	X1.4	2012 Jul 12 16:24	843	76	X	SEP
2013 Oct 25 14:51–15:12	X2.1	2013 Oct 25 15:12	1081	Halo	L	L
2013 Oct 29 21:42–22:01	X2.3	2013 Oct 29 22:00	1001	Halo	L	L
2013 Nov 5 22:07–22:15	X3.3	2013 Nov 5 22:36	562	195	L	L
2013 Nov 8 04:20–04:29	X1.1	L	L	L	L	L
2013 Nov 10 05:08–05:18	X1.1	2013 Nov 10 05:36	682	262	L	L
2013 Nov 19 10:14–10:34	X1.0	2013 Nov 19 10:36	740	Halo	L	L
2014 Mar 29 17:35–17:54	X1.0	2014 Mar 29 18:12	528	Halo	L	L
2014 Apr 25 00:17–00:38	X1.3	2014 Apr 25 00:48	456	296	X	L
2014 Jun 10 11:36–11:44	X2.2	2014 Jun 10 11:48	925	111	L	L
2014 Oct 19 04:17–05:48	X1.1	2014 Oct 19 06:12	170	43	L	L
2014 Oct 22 14:02–14:50	X1.6	L	L	L	X	L
2014 Oct 24 21:07–22:13	X3.1	2014 Oct 24 21:48	184	35	L	L
2014 Oct 25 16:55–18:11	X1.0	2014 Oct 25 17:36	171	49	L	L
2014 Oct 26 10:04–11:18	X2.0	L	L	L	X	L
2014 Oct 27 14:12–15:09	X2.0	2014 Oct 27 15:12	170	55	L	L
2014 Nov 7 16:53–17:34	X1.6	2014 Nov 7 17:12	469	87	L	L
2014 Dec 20 00:11–00:55	X1.8	L	L	L	X	L
2015 Mar 11 16:11–16:29	X2.2	2015 Mar 11 17:00	240	74	L	L
2015 May 5 22:05–22:15	X2.7	2015 May 5 22:24	715	Halo	L	L
2017 Sep 7 14:20–14:55	X1.3	2017 Mar 9 12:36	223	7	L	L

Note. The Fermi-LAT observable column indicates whether the prompt phase of the X-ray flare occurred within a SunMonitor time window. The SEP event column indicates the presence of this flare in the Major SEP Event list.

Solar eruptive events involve two distinct but related phenomena: (1) acceleration of electrons and ions at the reconnection regions in coronal loops that produce the impulsive nonthermal radiation observed from microwaves to γ rays, lasting several minutes, and are observed as impulsive-prompt SEPs, often with substantial enhanced abundances of ^{3}He and heavier ions. (2) Production of a supersonic CME which drives a shock, where particles are accelerated, resulting in long-duration SEPs with normal ionic abundances, with only one radiative signature of type II radio emission produced by less numerous SEP electrons. As summarized above, the Fermi-LAT observations show both prompt-impulsive γ-ray emission having lightcurves similar to those of the HXRs, and long-duration delayed emission with temporal behavior similar to SEPs, and like gradual SEPs, associated with fast CMEs. These similarities between gradual SEPs and >60 MeV gradual-delayed emission plus the observed drifting of the centroid of γ-ray emission from the original active region, which is accentuated by the observations of BTL flares, indicate that the site and mechanism of the acceleration of ions responsible for the long-duration γ rays is different from that of particles producing the impulsive nonthermal flare radiation and suggest that long-duration γ rays are another radiative signature of acceleration in CME shocks. However, unlike the type II radiation, they are produced by ions (accelerated in the CME-driven shock) and not in the low-density environment of the CME. While SEPs are particles escaping the upstream of the shock, the γ rays must be produced by ions escaping from the downstream region of the shock back to the high-density photosphere of the Sun, and because of the complex and changing magnetic connection between the CME and the Sun, sometimes to regions far from the AR from which the eruptions originated. The recent reconstruction of these magnetic connections by Jin et al. (2018) provides support for this scenario.

Alternative scenarios for explaining the gradual-delayed emission observed by Fermi have been put forth by authors such as De Nolfo et al. (2019) in their comparison between the characteristics of high-energy SEPs observed by PAMELA and those of the delayed-type emission γ-ray flares. One such scenario is that particles are accelerated via the second-order Fermi mechanism and trapped locally within extended coronal loops. These accelerated particles would then diffuse to the denser photosphere to radiate (Ryan & Lee 1991). With this approach, it is possible to decouple the acceleration of the particles producing γ rays from the acceleration and transport of the SEPs, allowing for different energetic particle productivities.

Thanks to the increase in sensitivity of the Fermi-LAT the sample of >100 MeV γ-ray flares has increased by almost a factor of 10 thus allowing us to perform population studies on these events for the first time. The observations presented in this work suggest that the particles producing the prompt-type emission and those producing the delayed-type emission are accelerated via different mechanisms. However, further multi-wavelength observations and in-depth simulations are needed in order to come to a definitive answer to which acceleration mechanism is driving the delayed-type γ-ray emission of solar flares.

The Fermi-LAT Collaboration acknowledges generous ongoing support from a number of agencies and institutes that have supported both the development and the operation of the LAT as well as scientific data analysis. These include the National Aeronautics and Space Administration and the Department of Energy in the United States, the Commissariat à l'Energie Atomique and the Centre National de la Recherche Scientifique/Institut National de Physique Nucléaire et de Physique des Particules in France, the Agenzia Spaziale Italiana and the Istituto Nazionale di Fisica Nucleare in Italy, the Ministry of Education, Culture, Sports, Science and Technology (MEXT), High Energy Accelerator Research Organization (KEK) and Japan Aerospace Exploration Agency (JAXA) in Japan, and the K. A. Wallenberg Foundation, the Swedish Research Council and the Swedish National Space Board in Sweden.

Additional support for science analysis during the operations phase is gratefully acknowledged from the Istituto Nazionale di Astrofisica in Italy and the Centre National d'Études Spatiales in France. This work performed in part under DOE contract DE-AC02-76SF00515.

M.P.R. and N.O. acknowledge relevant and helpful discussions with members of the ISSI International Team on Energetic Ions: The Elusive Component of Solar Flares and with participants in the Lorentz Center Workshop on Solar Sources of GeV Gamma-rays, 2018 February 26–March 2.

ORCID iDs

M. Ajello https://orcid.org/0000-0002-6584-1703
L. Baldini https://orcid.org/0000-0002-9785-7726
D. Bastieri https://orcid.org/0000-0002-6954-8862
R. Bellazzini https://orcid.org/0000-0002-2469-7063
E. Bissaldi https://orcid.org/0000-0001-9935-8106
R. D. Blandford https://orcid.org/0000-0002-1854-5506
C. C. Cheung https://orcid.org/0000-0002-4377-0174
F. D'Ammando https://orcid.org/0000-0001-7618-7527
Y. Fukazawa https://orcid.org/0000-0002-0921-8837
S. Funk https://orcid.org/0000-0002-2012-0080
P. Fusco https://orcid.org/0000-0002-9383-2425
F. Gargano https://orcid.org/0000-0002-5055-6395
D. Gasparrini https://orcid.org/0000-0002-5064-9495
M. Giroletti https://orcid.org/0000-0002-8657-8852
S. Guiriec https://orcid.org/0000-0001-5780-8770
E. Hays https://orcid.org/0000-0002-8172-593X
J. W. Hewitt https://orcid.org/0000-0001-5254-2248
M. Kuss https://orcid.org/0000-0003-1212-9998
S. Larsson https://orcid.org/0000-0003-0716-107X
F. Longo https://orcid.org/0000-0003-2501-2270
P. Lubrano https://orcid.org/0000-0003-0221-4806
S. Maldera https://orcid.org/0000-0002-0698-4421
A. Manfreda https://orcid.org/0000-0002-0998-4953
M. N. Mazziotta https://orcid.org/0000-0001-9325-4672
T. Mizuno https://orcid.org/0000-0001-7263-0296
M. E. Monzani https://orcid.org/0000-0002-8254-5308
A. Morselli https://orcid.org/0000-0002-7704-9553
I. V. Moskalenko https://orcid.org/0000-0001-6141-458X
N. Omodei https://orcid.org/0000-0002-5448-7577
M. Pesce-Rollins https://orcid.org/0000-0003-1790-8018
V. Petrosian https://orcid.org/0000-0002-2670-8942
J. L. Racusin https://orcid.org/0000-0002-4744-9898
R. Rando https://orcid.org/0000-0001-6992-818X
B. Rani https://orcid.org/0000-0001-5711-084X
M. Razzano https://orcid.org/0000-0003-4825-1629
S. Razzaque https://orcid.org/0000-0002-0130-2460
A. Reimer https://orcid.org/0000-0001-8604-7077
O. Reimer https://orcid.org/0000-0001-6953-1385
E. Troja https://orcid.org/0000-0002-1869-7817

References

Abdo, A. A., Ackermann, M., Ajello, M., et al. 2011, ApJ, 734, 116
Abeysekara, A. U., Archer, A., Benbow, W., et al. 2018, ApJ, 866, 24
Ackermann, M., Ajello, M., Albert, A., et al. 2012a, ApJS, 203, 4

Ackermann, M., Ajello, M., Albert, A., et al. 2014, ApJ, 787, 15
Ackermann, M., Ajello, M., Allafort, A., et al. 2012b, ApJ, 745, 144
Ackermann, M., Ajello, M., Baldini, L., et al. 2018, ApJS, 237, 32
Ackermann, M., Allafort, A., Baldini, L., et al. 2017, ApJ, 835, 219
Ahnen, M. L., Ansoldi, S., Antonelli, L. A., et al. 2019, MNRAS, 485, 356
Ajello, M., Albert, A., Allafort, A., et al. 2014, ApJ, 789, 20
Arnaud, K. A. 1996, in ASP Conf. Ser. 101, Astronomical Data Analysis Software and Systems V, ed. G. H. Jacoby & J. Barnes (San Francisco, CA: ASP), 17
Atwood, W., Albert, A., Baldini, L., et al. 2013, arXiv:1303.3514
Atwood, W. B., Abdo, A. A., Ackermann, M., et al. 2009, ApJ, 697, 1071
Barat, C., Trottet, G., Vilmer, N., et al. 1994, ApJL, 425, L109
Bruel, P., Burnett, T. H., Digel, S. W., et al. 2018, arXiv:1810.11394
Chupp, E. L. 1987, PhST, 18, 5
Chupp, E. L., Forrest, D. J., Ryan, J. M., et al. 1982, ApJL, 263, L95
Chupp, E. L., & Ryan, J. M. 2009, RAA, 9, 11
Cliver, E. W., Kahler, S. W., & Vestrand, W. T. 1993, ICRC (Calgary), 23, 91
De Nolfo, G., Bruno, A., Ryan, J., et al. 2019, ApJ, 879, 90
Dennis, B. R. 1988, SoPh, 118, 49
Di Mauro, M., Manconi, S., Zechlin, H. S., et al. 2018, ApJ, 856, 106
Dolan, J. F., & Fazio, G. G. 1965, RvGeo, 3, 319
Forrest, D. J., Vestrand, W. T., Chupp, E. L., et al. 1985, ICRC (La Jolla), 19, 146
Forrest, D. J., Vestrand, W. T., Chupp, E. L., Rieger, E., & Cooper, J. 1986, AdSpR, 6, 115
Hurford, G. J., Krucker, S., Lin, R. P., et al. 2006, ApJL, 644, L93
Jin, M., Petrosian, V., Liu, W., et al. 2018, ApJ, 867, 122
Kanbach, G., Bertsch, D. L., Fichtel, C. E., et al. 1993, A&AS, 97, 349
Kocharov, L., Pesce-Rollins, M., Laitinen, T., et al. 2020, ApJ, 890, 13
Lin, R. P., & Team, Rhessi 2003, AdSpR, 32, 1001
Linden, T., Zhou, B., Beacom, J. F., et al. 2018, PhRvL, 121, 131103
Mattox, J. R., Bertsch, D. L., Chiang, J., et al. 1996, ApJ, 461, 396
Mazziotta, M. N., Luque, P. D. L. T., Di Venere, L., et al. 2020, PhRvD, 101, 083011
Meegan, C., Lichti, G., Bhat, P. N., et al. 2009, ApJ, 702, 791
Moskalenko, I. V., Porter, T. A., & Digel, S. W. 2006, ApJL, 652, L65
Murphy, R. J., Dermer, C. D., & Ramaty, R. 1987, ApJS, 63, 721
Nitta, N. V., Aschwanden, M. J., Boerner, P. F., et al. 2013, SoPh, 288, 241
Omodei, N., Pesce-Rollins, M., Longo, F., Allafort, A., & Krucker, S. 2018, ApJL, 865, L7
Orlando, E., & Strong, A. W. 2007, Ap&SS, 309, 359
Orlando, E., & Strong, A. W. 2008, A&A, 480, 847
Pesce-Rollins, M., Omodei, N., Petrosian, V., et al. 2015, ApJL, 805, L15
Poluianov, S. V., Usoskin, I. G., Mishev, A. L., Shea, M. A., & Smart, D. F. 2017, SoPh, 292, 176
Reames, D. V. 1995, AdSpR, 15, 41
Ryan, J. M. 2000, SSRv, 93, 581
Ryan, J. M., & Lee, M. A. 1991, ApJ, 368, 316
Sakurai, T. 2008, The Hinode Mission (Berlin: Springer)
Seckel, D., Stanev, T., & Gaisser, T. K. 1991, ApJ, 382, 652
Shih, A. Y., Lin, R. P., & Smith, D. M. 2009, ApJL, 698, L152
Shrivastava, P. K., & Singh, N. 2005, ChJAA, 5, 198
Thompson, D. J., Bertsch, D. L., Fichtel, C. E., et al. 1993, ApJS, 86, 629
Trottet, G., Vilmer, N., Barat, C., et al. 1998, A&A, 334, 1099
Vestrand, W. T., & Forrest, D. J. 1993, ApJL, 409, L69
Vianello, G., Lauer, R. J., Younk, P., et al. 2015, arXiv:1507.08343
Vilmer, N. 1987, Hard X-ray Emission Processes in Solar Flares (Springer Netherlands: Dordrecht), 207
Vilmer, N., MacKinnon, A. L., & Hurford, G. J. 2011, SSRv, 159, 167
Vilmer, N., MacKinnon, A. L., Trottet, G., & Barat, C. 2003, A&A, 412, 865
Vilmer, N., Trottet, G., Barat, C., et al. 1999, A&A, 342, 575
Wood, M., Caputo, R., Charles, E., et al. 2017, ICRC (Busan), 35, 824